UNIVERSITY OF CALIFORNIA

Los Angeles

Interaction of a Relativistic Electron Beam with Radiation in the THz Frequency Range

A dissertation submitted in partial satisfaction of the

requirements for the degree Doctor of Philosophy

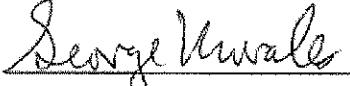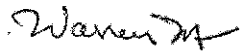in Electrical Engineering

by

Chieh Sung

2008

ii

The dissertation of Chieh Sung is approved.

Francis F. Chen

George Morales

Warren Mori

Chan Joshi, Committee Chair

University of California, Los Angeles

2008

DEDICATION

To my father, Ting-Hsiung.

Table of Contents

List of Figures

List of Tables

VITA

1975   Born, Taipei, Taiwan

1997   B.S. (Physics), National Taiwan University, Taipei, Taiwan

2000   Teaching Assistant, Physics Department, National Tsing-Hua University

2001   M.S. (Physics), National Tsing-Hua University, Hsin-Hsu, Taiwan

2004   M.S. (Electrical Engineering), UCLA

2001-Present Graduate Research Assistant, Neptune Laboratory, Electrical Engineering
            Department, UCLA

Publications

C. Sung, S. Ya. Tochitsky, and C. Joshi, " Guiding of 10 μm laser pulses by use of hollow waveguides," Advanced Acceleration Concepts, 2004, edited by V. Yakimenko, AIP conf. Proc. pp. 922-928 (2004)

C. Sung, S. Ya. Tochitsky, P. Musumeci, et al, " Study of a THz IFEL prebuncher for laser-plasma accelerators," Advanced Acceleration Concepts, 2004, edited by V. Yakimenko, AIP conf. Proc. pp. 922-928 (2004)

P. Musumeci, S. Ya. Tochitsky, S. Boucher, A. Doyuran, R. J. England, C. Joshi, C. Pellegrini, J. Ralph, J. B. Rosenzweig, C. Sung, S. Tolmachev, G. Travish, A. A.

Varfolomeev, A. A. Varfolomeev Jr., T. Yarovoi, and R. B. Yoder, " Very high energy gain at the Neptune Inverse Free Electron Laser Experiment," Advanced Acceleration Concepts, 2004, edited by V. Yakimenko, AIP conf. Proc. pp. 160 (2004)

C. Sung, S. Ya. Tochitsky, S. Reiche, et al, " High gain seeded FEL Amplifier Tunable in the Terahertz Range," Proceedings of the 27th International Free Electron Laser Conference 2005, pp.87 –90 (2005)

C. Sung, S. Ya. Tochitsky, J. Ralph, et al, " TeraHertz IFEL/FEL microbunching for plasma beat-wave accelerators," 2007 IEEE Particle Accelerator Conference. IEEE. TPAE004. (2005)

S. Ya. Tochitsky, J. E. Ralph, C. Sung, et al, "Generation of magawatt-power terahertz pulses by noncollinear difference-frequency mixing in GaAs," J. Appl. Phys. 98, 026101 (2005)

P. Musumeci, S. Ya. Tochitsky, S. Boucher, C. E. Clayton, A. Doyuran, R. J. England, C. Joshi, C. Pellegrini, J. Ralph, J. B. Rosenzweig, C. Sung, S. Tolmachev, G. Travish, A. A. Varfolomeev, A. A. Varfolomeev Jr., T. Yarovoi, and R. B. Yoder, "High energy gain of trapped electrons in a tapered, diffraction-dominated inverse-free-electron-laser," Phys. Rev. Lett., 94, 154801 (2005)

C. Sung, S. Ya. Tochitsky, S. Reiche, et al, " Development of a Waveguide FEL seeded in the 1-3 THz range for Microbunching Experiment at the Neptune Laboratory," Advanced Acceleration Concepts, 2006, edited by M. Conde and C. Eyberger, AIP conf. Proc. pp. 895-902 (2006)

S. Ya. Tochitsky, C. Sung, S. Trubnick, and C. Joshi, " Narrow-band. Intense Terahertz pulses from a large aperture GaAs frequency downconverter," Conference on Lasers and Electro-Optics 2006 Technical Digest (Optical society of America, Washington DC, 2006) Ctu664

C. Sung, S. Ya. Tochitsky, S. Reiche, J. B. Rosenzweig, C. Pellegrini, and C. Joshi et al, " Seeded free-electron and inverse free-electron laser techniques for radiation amplification and electron microbunching in the terahertz range," Phys. Rev. ST Accel. Beams 9, 120703 (2006)

S. Ya. Tochitsky, S. Reiche, C. Sung, J. B. Rosenzweig, C. Pellegrini, and C. Joshi, " Laser Beat-Wave microbunching of relativistic electron beam in the THz range," Proceedings of LINAC 2006, MOP029

S. Ya. Tochitsky, C. Sung, S. E. Trubnick, C. Joshi, and K. L. Vodopyanov, "High-power tunable, 0.5-3 THz radiation source based on nonlinear difference frequency mixing of CO laser lines", J. Opt. Soc. Am. B, Vol. 24, No. 9, pp. 2509-2516 (2007)

ABSTRACT OF THE DISSERTATION

Interaction of a Relativistic Electron Beam with

Radiation in the THz frequency Range

by
Chieh Sung

Doctor of Philosophy in Electrical Engineering

University of California, Los Angeles, 2008

Professor Chan Joshi, Chair

The ability to generate a train of microbunches that are only typically tens of

femtosecond wide and are separated by a picosecond is a topic of contemporary interest in

the field of free electron lasers and plasma based accelerators. Moreover the usefulness of

the high gradients present in plasma accelerators will depend on the ability to obtain

mono-energetic relativistic electrons. This means that in addition to being prebunched on

on a scale shorter than the plasma wavelength the externally injected electron beam must

be phase-locked to the accelerating plasma wave structure. In this thesis we investigate

two techniques, Free Electron Laser interaction (FEL) and the Inverse Free Electron Laser

interaction (IFEL), by which a medium energy electron beam can be prebunched into a

series of microbunches with the same periodicity as a plasma wave and is phase locked to it.

Using full- scale, 3-D simulations we show in this thesis that when a relativistic electron beam and an electromagnetic wave propagate collinearly through a magnetic undulator, FEL and IFEL interactions have the capability to form electron microbunches with periodicity 300-100 μm (1-3 THz range), which contain 50% of electrons within a small fraction of the ponderomotive buckets. Such a bunched beam is suitable for injection into plasma densities in the range 10^{16}-10^{17} cm^{-3}, respectively. Microbunching using the FEL mechanism requires a narrowband THz radiation source to act as a seed whereas the IFEL mechanism requires, in addition, such a source to be high power. In this thesis the generation of THz radiation in the Neptune Laboratory by mixing of two CO_2 laser lines in a non-collinearly phase matched GaAs at room temperature is described A high-power THz pulse with up to 2 MW of peak power in a 250 ps pulse was generated using a TW class CO_2 laser pulse. Such high power THz radiation is needed for the IFEL approach to microbunching. We also produced a high repetition rate THz source tunable in the 0.5-3 THz range with a maximum of ~2 kW of peak power in a 200 ns pulse suitable as a seed for an FEL microbuncher. These sources represent the most powerful and the most energetic narrowband THz sources currently reported using nonlinear optical technique to our knowledge.

During the FEL microbunching process, the wiggling electrons in the undulator also emit radiation coherently at the resonant frequency; as a result, the THz FEL microbuncher can double as a single pass THz amplifier tunable in the 0.5-3 THz range. It

is shown that when seeded with a ~1 kW THz pulse and driven by an electron beam with a peak current of 60A, a 2 m-long undulator can amplify the radiation power to ~20MW. The frequency range can be further expanded to up to 9 THz via the High Gain Harmonic Generation (HGHG) FEL configuration. The results of these simulations are used as a guide in designing a single-pass THz FEL microbuncher/amplifier which is currently under construction.

In order to study THz microbunching and amplification, several original techniques and diagnostics were also developed. Guiding a THz pulse through a hollow waveguide, filtering a short THz pulse using a Fabry-Perot interferometer and measuring the frequency components using a diffraction grating spectrometer were demonstrated.

1. Introduction

A laser driven plasma accelerator has the potential for providing high-energy electron beams at a fraction of the current cost of a standard RF-based accelerator [1-5]. Recently, self-trapped plasma electrons were accelerated to 0.3-1GeV in a 5-8mm long relativistic plasma wave structure using a short pulse laser driver [6]. In spite of the demonstrated high-gradients, the potential of a laser-plasma accelerator for the next generation of accelerators that will require staging of many such schemes of laser acceleration cannot be ascertained without solving the issue of matching of a particle beam into the plasma accelerating structure and efficient extraction of this beam from such a structure. This is important for acceleration of a reasonable amount of charge (~nC) with a narrow energy spread. To study these issues, we introduce a Plasma LINAC concept in which the injected particles are pre-bunched on a scale shorter than the wavelength of the accelerating structure but with the same periodicity as the plasma wave such that monoenergetic acceleration of electrons can be obtained [7]. For example, for a plasma wave resonantly driven at plasma densities in the range 10^{16}-10^{17} cm^{-3}, the plasma wavelength λ_p is equal to 340-100 μm (1-3 THz), respectively. In order to inject electrons into a narrow phase interval of such plasma waves, an electron beam needs to be prebunched into a series of ~50-15 μm long microbunches separated by the plasma wavelength.

In order to develop the Plasma LINAC concept further, we have carried out a series of studies in order to investigate THz microbunching. A relativistic electron beam can be modulated on the radiation wavelength scale via Free Electron Laser (FEL) mechanism while co-propagating in the periodic magnetic field [8]. Another scheme is called Inverse

Free Electron Laser (IFEL) and was successfully demonstrated at 10 μm in the STELLA experiment [9]. However, the IFEL technique requires a very strong external laser field, which is not available in the THz range. The main motivation of this dissertation was: i) to study THz IFEL/FEL microbunching numerically, ii) to determine requirements for magnetic devices (undulators) and radiation sources, and iii) to develop high-power seed sources operating in the 1-3 THz range.

In Chapter 2, we visit both IFEL and FEL theories and compare these two microbunching techniques. In Chapter 3, the conceptual scheme for Plasma LINAC is described, and we examine IFEL and FEL approaches for obtaining microbunched electrons using simulation codes. First, we designed an undulator with optimal parameters for THz IFEL using a photoinjector-based electron beam. Then we modeled the THz IFEL effect using a 3-D simulation code *TREDI* [10] and estimated the power requirement for the external THz radiation. Then, we applied FEL microbunching technique and determined the seed power requirement using another 3-D code *GENESIS 1.3* [11].

Another aspect of interaction between the electron beam and seeded radiation pulse is amplification of the radiation pulse. In a FEL, the wiggling electrons also emit THz radiation with the same wavelength as the seed coherently. Note that up to date, the most powerful narrowband ($\Delta v/v \sim$ 1-10%) THz radiation source is an ~1MW FEL at the FELIX user facility, Netherlands [12], in which a multi-pass FEL oscillator is driven by a few microsecond long electron beam with low peak current and the radiation is amplified from spontaneous noise. A more compact, high power THz source using a shorter undulator and driven by a photoinjector electron beam will be very useful for the scientific community.

Here we propose to use a seeded single-pass FEL amplifier which can significantly shorten the undulator length, thus opening the possibility of driving FELs with a short, high peak current beam and reach a very high FEL gain [13]. In Chapter 4, we present our numerical studies on a seeded FEL amplifier.

However, in the THz range, a seeded FEL amplifier is not yet studied experimentally due to the lack of a suitable radiation seed source. There are challenges in developing high power THz sources in this spectral range. Electronic techniques developed in the microwave range are difficult to extend beyond 200 GHz due to the limitation in reducing physical sizes; on the other hand, optical techniques of quantum electronics are difficult to extend below 10 THz because the photon energies are smaller than typical transition energies. The most successful techniques for generating narrow-band, high-power THz pulses have come from frequency down-conversion of the nanosecond 1-μm or 10-μm lasers in nonlinear crystals. Tunable Difference Frequency Generation (DFG) in the THz range was demonstrated both in birefringent, e.g., $ZnGeP_2$ [14,15], $LiNbO_3$ [16,17] and GaSe [18] and isotropic, e.g., GaAs [19] nonlinear materials. In this dissertation, we have explored the use of a comb of CO_2 laser lines to generate a narrow-band pulse in the THz range of 100-340 μm through DFG in a GaAs crystal. In Chapter 5, the development of high repetition rate and high power THz seed sources in the Neptune Laboratory are shown.

The THz range of spectrum is completely underdeveloped in terms of measurement techniques and optical components. In Chapter 6, we describe development of several THz optical devices and their applications for experimental measurements. It is known

3

that due to the longer wavelength, compared to an optical pulse, the THz radiation diffracts much faster. Therefore, guiding of the THz pulse is needed to reduce the diffraction losses during propagation. We report guiding of a THz pulse in metallic waveguides and discuss possible solutions to reduce losses. One challenge in obtaining a high contrast ratio THz pulse from the seeded FEL amplifier is separation of the short amplified pulse from the original long seed pulse. A Fabry-Perot interferometer optimized for the THz radiations is built to separate pulses with different durations. In our Fabry-Perot filter, a long pulse is transmitted thru the interferometer and dumped, however, the short pulse is reflected and can be used for experiments. As for diagnostics, we have also developed a THz spectrometer based on diffraction gratings. The spectrometer was built and calibrated using our high repetition rate THz source.

THz seeded FEL/IFEL experimental studies require use of a precise periodic magnet-undulator, building of which requires professional expertise. At present, collaboration with STI Optronics on undulator design/modeling and manufacture is in progress and steps toward the experiments on FEL will be continued beyond this dissertation. We cover in the final part of Chapter 6 the status of the THz FEL amplifier/buncher project at the Neptune Laboratory.

2. Theory of IFEL and FEL in THz range

2.1 Introduction of FEL/IFEL interactions

An Inverse Free-Electron Laser (IFEL) and a Free-Electron Laser (FEL) are terms that are used historically to distinguish two common techniques for modulating the energy of an electron beam on a certain radiation wavelength. However, an IFEL is essentially a special case of the more generic FEL mechanism.

A Free-Electron Laser differs from common type of lasers because the electrons are not bound to quantum states of an optical medium but to a magnetic system instead. The electrons pass the alternating magnetic field of an undulator or wiggler thus being forced to oscillate transversely. The motion causes the emission of radiation, called spontaneous undulator emission, sharply peaked at resonant frequencies. The emission can be stimulated by the presence of an external radiation field; therefore, the FEL can be classified as a laser with the additional feature that the radiation frequency is tunable by varying the electron beam energy.

There are three types of operation of FELs: FEL amplifier, Self-Amplified Spontaneous Emission (SASE) FEL and FEL oscillator.

When an external radiation field seeds the FEL and gets amplified by the interaction with the electron beam, it is called the FEL amplifier. The FEL amplifier is the simplest device to understand FEL physics, and is the focus of this thesis.

A SASE FEL operates almost like an FEL amplifier; the only difference is that the seeding field is supplied by the spontaneous emission. Because the bandwidth of the spontaneous emission spectrum is larger than that of the FEL amplification, the SASE

5

FEL is always tuned to the resonant frequency, which has the largest growth rate. The disadvantage is that the radiation pulse consists of spikes caused by the random fluctuation in the longitudinal electron positions. And normally a longer undulator is required for the SASE regime.

A FEL oscillator is a device when the undulator is enclosed by mirrors to provide a feedback cavity and the radiated photons are reflected back to the entrance of the undulator. The characteristics of the FEL, such as the transverse size of the radiation field and the synchronization between the radiation pulse and the electron beam, are strongly influenced by the optical cavity. Gain here also starts from the spontaneous emission of the electron beam.

In a FEL, the energy transfer is mostly from the electron beam to the electromagnetic (EM) wave. However, in a special case of the seeded FEL amplifier, when the external radiation seed is several orders of magnitude stronger than the spontaneous undulator emission, the net energy transfer is from the external radiation fields to the electron beam. Because the electron beam gains energy in this special case, it is conventionally called Inverse Free-Electron Laser. In the IFEL, only the charged particle motion under EM fields is considered; thus its simplicity provides a clear physical picture of the energy modulation of the electron beam in the FEL process.

This chapter gives an overview of the FEL mechanism. Starting from explaining the IFEL interaction (Section 2.2), then we consider the spontaneous undulator emission and describe the whole FEL process afterwards (Section 2.3). This chapter introduces the basic knowledge of FEL and establishes the foundation for simulations and experiments

FEL is always tuned to the resonant frequency, which has the largest growth rate. The disadvantage is that the radiation pulse consists of spikes caused by the random fluctuation in the longitudinal electron positions. And normally a longer undulator is required for the SASE regime.

A FEL oscillator is a device when the undulator is enclosed by mirrors to provide a feedback cavity and the radiated photons are reflected back to the entrance of the undulator. The characteristics of the FEL, such as the transverse size of the radiation field and the synchronization between the radiation pulse and the electron beam, are strongly influenced by the optical cavity. Gain here also starts from the spontaneous emission of the electron beam.

In a FEL, the energy transfer is mostly from the electron beam to the electromagnetic (EM) wave. However, in a special case of the seeded FEL amplifier, when the external radiation seed is several orders of magnitude stronger than the spontaneous undulator emission, the net energy transfer is from the external radiation fields to the electron beam. Because the electron beam gains energy in this special case, it is conventionally called Inverse Free-Electron Laser. In the IFEL, only the charged particle motion under EM fields is considered; thus its simplicity provides a clear physical picture of the energy modulation of the electron beam in the FEL process.

This chapter gives an overview of the FEL mechanism. Starting from explaining the IFEL interaction (Section 2.2), then we consider the spontaneous undulator emission and describe the whole FEL process afterwards (Section 2.3). This chapter introduces the basic knowledge of FEL and establishes the foundation for simulations and experiments

discussed in the following chapters.

2.2 IFEL theory

To describe the IFEL interaction, we choose "linearly polarized EM wave and planar undulator" configuration (as shown in Figure 2.1), since all of the work included in this dissertation considers a planar geometry.
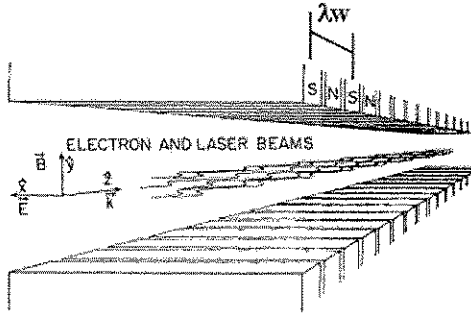
Figure 2.1: Schematics of an IFEL interaction

An undulator is an array of permanent magnets with their polarization alternatively aligned along the y-axis (Fig 2.1). When electrons wiggle along the axis of such an undulator (on the x-z plane), an external EM wave with linearly-polarization (x-direction) can modulate the energy of electrons due to the non-zero product of the electric field and the electron velocity.

Starting from Lorentz force equations and transverse canonical momentum conservation, we can derive IFEL equations of motion in a planar IFEL undulator using the 1 dimensional approximation as in [20]:

$$\frac{\partial \gamma}{\partial z} = \frac{kKK_L}{\gamma} \cdot \frac{JJ}{2} \sin(\psi) \tag{2.1}$$

8

$$\frac{\partial \psi}{\partial z} = k_w - k \cdot \frac{1 + K^2/2 + K_L^2/2 + KK_L \cdot JJ \cdot \cos(\psi)}{2\gamma^2} \qquad (2.2)$$

where γ is the electron energy, k the radiation wave number, and k_w the undulator wave number; K_L is the radiation dimensionless parameter (eE_o/mc^2k), K is the undulator dimensionless parameter ($K=eB_w/mc^2k_w$, where B_w is the undulator magnetic field), Ψ is the phase of coupling between the wiggling motion and the EM wave ($\Psi=$ (k+k$_w$)z-ωt), and JJ is the coupling factor, which is a function of the undulator normalized strength K. Normally, the IFEL is designed in such a way that only the first term of all JJ factors is important. Therefore, JJ = [$J_0(G)$ - $J_1(G)$], where J_n are the Bessel function of first kind and G=(1+K^2/2)K^2/4. Note that, as seen in Eq. 2.1, for a given electron energy γ and same radiation power, the larger the K of the undulator, the stronger the energy modulation is imposed on the electrons.

An arbitrary choice of parameters is unlikely to produce much net energy modulation because the phase Ψ will vary over a large range and the acceleration term will change sign quickly. To maximize the efficiency of the energy exchange, parameters are chosen such that the phase Ψ stays constant, it is called *resonant condition*. Thus Eq. 2.2 becomes:

$$\lambda = \frac{\lambda_w}{2 \cdot \gamma^2} \cdot \left(1 + \frac{K^2}{2}\right) , \qquad (2.3)$$

where λ is the radiation wavelength, and λ_w the undulator wavelength. Physically, it means that under the resonant condition the radiation outruns the electron beam by one wavelength when the electron beam in the undulator wiggles one period.

2.3 FEL theory and longitudinal dynamics of electron beam

The energy of the electron beam can be modulated by interaction with the EM wave in the undulator and this energy modulation leads to bunching of electrons as described in the previous session. In a FEL, besides such interaction, the spontaneous undulator emission generated by wiggling electron bunches should also be taken into account. Under the resonant condition, this newborn radiation is emitted coherently with the seed radiation, thus the amplification of the EM wave occurs. Subsequently, the amplified EM wave modulates the electron energy further more; as a result, it forms a full positive FEL feedback loop and the EM wave grows exponentially. The electron beam parameters such as the peak current and emittance are important in a FEL, because it plays a major role in the positive feedback mechanism. The net FEL energy exchange is from the electron beam to the EM wave. Eventually, the EM wave power reaches saturation because electrons lose too much energy and are no longer in resonance.

Because the FEL mechanism is the combination of energy modulation of the electron beam and amplification of the radiation, it can be used as a radiation source as well as a microbuncher, a device producing a longitudinally modulated electron beam.

To illustrate the THz power and the modulation of the electron beam at different stages of the FEL process, we show a typical plot of radiated power dependence upon the undulator length in Fig. 2.3. In the first few periods of the undulator, the seed radiation modulates the electron beam slightly (linear gain stage in Fig. 2.3) and the radiation power grows very slowly. As the energy-modulated electron beam becomes more and more bunched, it radiates coherently to amplify the radiation, which further modulates the

12

electron beam energy (exponential gain stage in Fig. 2.3). This positive feedback leads to an exponential gain of the radiation power.
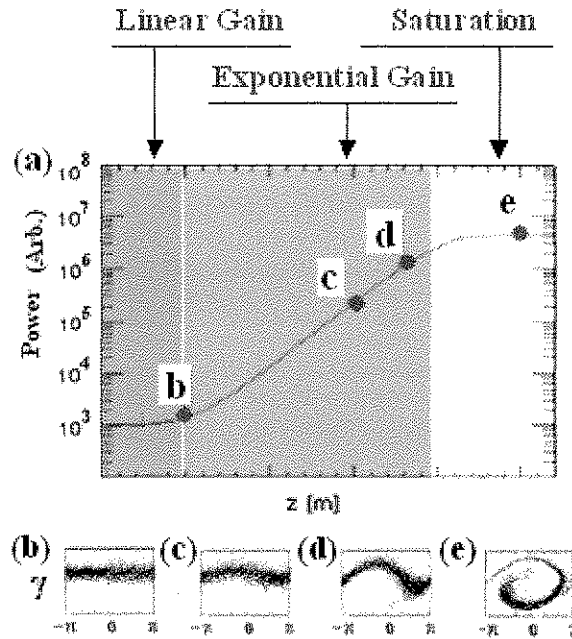
Figure 2.3: THz power as a function of the undulator length z (a) and the phase distribution of electrons in one radiation wavelength at four different positions (b through e)

A correlation between the THz power and the bunching of electrons is clear when we look into the phase distribution of electrons at various positions (in Fig. 2.3(b), (c), (d), (e)): the energy modulation increases along with the amplification of the radiation. Eventually, electron phase-space starts folding and electrons become trapped in the ponderomotive bucket (see Fig. 2.3(e)). At position (e), the electron beam losses too much energy and is out of resonance such that the THz power is saturated. Note that the K factor and/or undulator wavelength λ_w can be tapered along the undulator to keep the resonant

condition valid as the particles lose energy to the EM wave. By doing so, the saturation happens later and the slope of the FEL gain can be preserved [21].

In terms of FEL microbunching, the most favorable is position (d) in Fig. 2.3 where the energy modulation is optimal and folding has yet to occur. In order to transfer the energy modulation to the current modulation, ballistic drifting of the beam over a distance of a meter or using a chicane is necessary.

2.4 Summary of FEL and IFEL

We summarize briefly characteristic features of FEL and IFEL in Table 1.
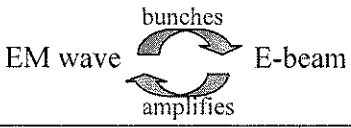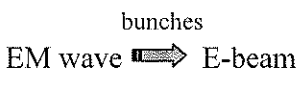
	FEL	IFEL
Net Energy exchange	EM wave $\Leftarrow$ E-beam	EM wave $\Rightarrow$ E-beam
Seed power level	Small ($< P_{saturation}$)	Large ($>> P_{saturation}$)
	EM wave $\overset{bunches}{\rightleftarrows}$ E-beam amplifies	EM wave $\overset{bunches}{\Rightarrow}$ E-beam
Final radiation power level	Radiation power grows while bunching occurs	Radiation field is almost not changed
Method to enhance energy modulation	Higher E-beam current Higher EM wave intensity	Higher EM wave intensity

Table 1: Comparison between IFEL and FEL

To effectively transfer the energy between an EM wave and an electron beam, both a FEL and an IFEL need to satisfy the same resonant condition (Eq 2.3). Therefore, basic undulator design for FEL and IFEL is the same.

In non-seeded FEL interactions (an oscillator and SASE), the radiation starts from spontaneous noise and it is positive feedback mechanism that eventually results in a high-power radiation and a fully modulated electron beam. In a FEL amplifier, the radiation seed is amplified via the same mechanism and high power can reach sooner in the undulator due to a stronger initial radiation power level. However, when the initial radiation power level well exceeds the saturation power such that the spontaneous emission is negligible and the net energy exchange is from the EM wave to the electron

beam, an IFEL approximation discussed in Section 2.2 is valid. Therefore, the main difference between these two regimes is the level of EM wave power at the entrance of the undulator. As the result, the direction of the net energy transfer is opposite in an IFEL and a FEL. Note that for microbunching applications, an IFEL always requires an undulator with number of periods smaller than a FEL.

Thus in this chapter, we show that both IFEL and FEL techniques have potential for energy modulation of a relativistic electron beam. However, there are many specific issues when IFEL/FEL techniques are used in the THz range, such as seed radiation sources and the slippage effect between a short electron beam and a long wavelength radiation. We will discuss specifics of IFEL/FEL techniques in the THz spectral range in following chapters by using numerical simulations.

3. THz Microbunching via IFEL and FEL

3.1 Feasibility study of THz microbunching in Neptune Lab

The main goal of this thesis is to study techniques for modulation of a relativistic electron beam on the scale a plasma accelerator. This is important for external injection in plasma of multiple short electron beams with duration of a fraction of the plasma accelerating structure and with the same periodicity. For a plasma wave resonantly driven at plasma densities 10^{16}-10^{17} cm^{-3} (plasma wavelength λ_p is equal to 340-100 μm respectively), an electron beam needs to be prebunched into a series of ~50-15 μm long microbunches that separated by the plasma wavelength.
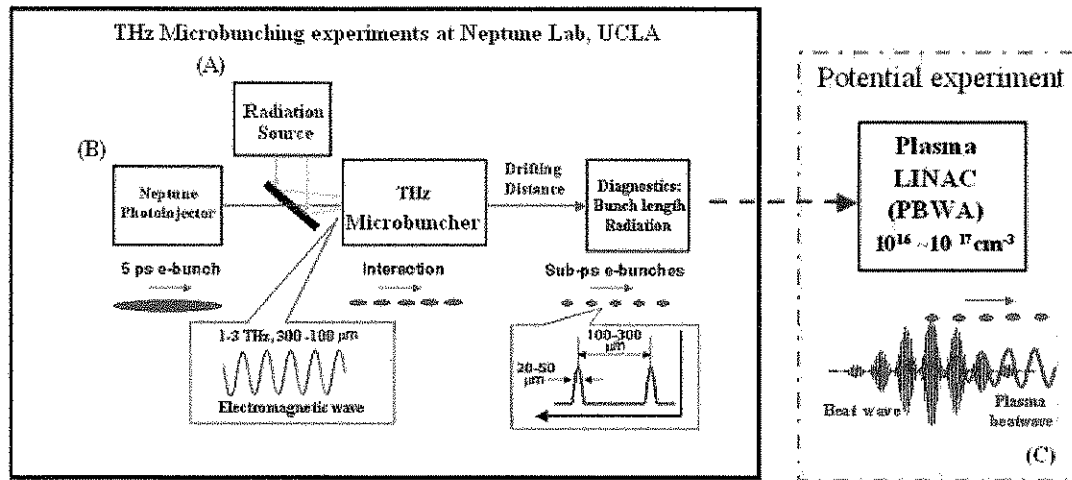
Figure 3.1: Schematics of THz microbunching experiments at Neptune Lab, UCLA

The concept of THz microbunching experiments at Neptune Laboratory is shown in Fig. 3.1. In the Plasma Beat-Wave Acceleration (PBWA) experiment at Neptune, two lines of a CO_2 laser (10.6 and 10.3 μm) were used to excite a relativistic plasma beat wave (λ_p

=340 μm) with an acceleration gradient ~ 1-3 GeV/m [22]. As explained in Chapter 2, both IFEL and FEL techniques can be used to microbunch a relativistic electron beam. We would like to study both THz IFEL and FEL microbunching in order to choose the optimal technique. Both techniques must produce a modulated electron beam phase-locked to the CO_2 laser beatwave. In the THz microbunching experiment, THz radiation which itself is phase-locked to the laser beat wave should be used to seed a planar undulator prebuncher. The electron beam coming from a photoinjector will interact with the THz radiation via IFEL/FEL mechanism while going through the undulator and get bunched while drifting in free space. After drifting, the bunched beam will be analyzed using different bunch length diagnostics, such as CTR measurements, and a RF cavity deflector [23]. It is important that on the THz scale direct measurement of longitudinal dynamics of electron bunches is still possible. However, the lack of a narrow-band, high power radiation source tunable in the 340-100 μm (1-3 THz) range makes THz microbunching a challenging topic to study.

The comb of CO_2 laser lines is an ideal source for generating step tunable, narrow-band radiation in the THz range of 100-1000 μm through difference frequency generation (DFG) in a nonlinear crystal. Thus there is a strong motivation both to develop a DFG-based source of THz radiation and to use it for microbunching at the range of interest of laser-plasma accelerators in the 10^{16}-10^{17} cm^{-3} density range. In Chapter 5, we will describe THz DFG in details and also show experimental results on high-power THz radiation sources. In this chapter, the main focus is to study the feasibilities of IFEL and FEL THz microbunching by using simulation codes and to determine the THz radiation

power requirements for both cases.

In Section 3.2, and 3.3, we show simulation results for THz IFEL and FEL microbunching, respectively. Different codes were used: the 3-D *TREDI* code models the particle motions of the IFEL interaction and energy transfer from the radiation pulse to electrons; the 3-D code *GENESIS 1.3* takes into account energy transfer from particles to the radiation and models all aspects of the FEL interactions. A summary and issues regarding the implementation of both techniques into experiments are discussed in Section 3.4.

3.2 3-D IFEL simulation code *TREDI* and microbunching results

In an IFEL, the intensity of the external radiation is critical to the energy modulation of electrons. Therefore, the IFEL effect drops significantly once the electron beam passes few Rayleigh lengths (Z_r) away from the waist of the radiation (w_0, and note that $Z_r = \pi w_0^2 / \lambda$). In a diffraction-dominated THz IFEL, the interaction is limited to only few Z_R due to the shorter Rayleigh length in the THz range. Therefore, instead of a diffraction-dominated IFEL, a waveguide IFEL configuration is considered here for THz microbunching. The waveguide is used for guiding and preserving the intensity of the THz radiation over a distance much longer than the Rayleigh length inside the undulator. As a result, a much lower power of the external THz radiation is needed to have the same amount of energy modulation.

However, note that the resonant condition (Eq. 2.3) corresponds to the free-space case. If the radiation propagates in a waveguide, Eq. 2.3 can be modified by replacing λ with the effective radiation wavelength (λ_{eff}) derived from the dispersion relation of the guiding structure. Practically, the resonant condition for a waveguide case can also be satisfied by scanning the electron energy γ.

The first step to simulate an IFEL is to optimize undulator parameters. It can be done by using analytical formulas and Fig. 3.2 illustrates the processes of optimization of undulator parameters for a waveguide IFEL.

As seen in Fig. 3.2, when $\lambda = 340$ μm, and $\gamma = 20$, the resonant condition (Eq. 2.3) is represented by the solid red curve and different K values are represented by dashed curves. Therefore, in order to maximize the energy modulation, λ_w and B_w are chosen along the

red solid to satisfy the resonant condition and to make K as large as possible.

$$B\max = 3.33 \cdot Exp\left[-\frac{Gap}{\lambda_w} \cdot (5.47 - 1.8 \cdot \frac{Gap}{\lambda_w})\right]$$
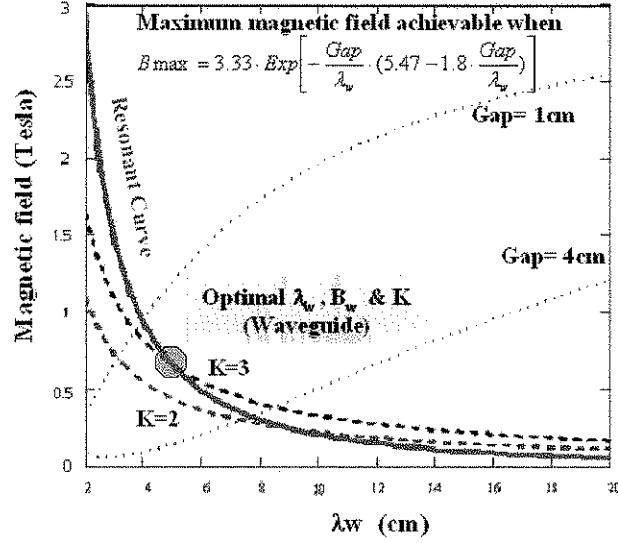
Figure 3.2: Optimization of the waveguide IFEL undulator (λ= 340 μm, γ= 20)

However, the Halbach formula (dotted curves in Fig. 3.2,

$$B\max = 3.33 \cdot Exp\left[-\frac{Gap}{\lambda_w} \cdot (5.47 - 1.8 \cdot \frac{Gap}{\lambda_w})\right] \qquad (3.1)$$

where Bmax is the maximum magnetic strength reachable, and Gap is the distance between poles of a magnet set limits the choices because of the physical restriction in building magnets with small periods.

In a waveguide IFEL, the gap between the magnets is set to accommodate a hollow waveguide inside the undulator. The waveguide inner diameter (ID) is chosen such that the propagating mode size can cover the whole wiggling electron beam inside the waveguide. After few iterations, we chose an undulator with a 1 cm gap, a waveguide ID of 8mm, λ_w=5cm, and B_w=0.66 T (K=3) for simulations in the waveguide IFEL case when

21

using $\lambda = 340$ μm and $\gamma = 20$.

There are two codes that we use to optimize the undulator design and to model the IFEL bunching effect. The 1-D code solves the equations of motions (Eq. 2.1 and 2.2) and calculates the phase and energy of each electron at any longitudinal position. The other is a 3-D code called TREDI that calculates the Lorenz force acting on each electron and also calculates its position and energy along time. We first roughly determined parameters of the undulator using the 1-D code and then finalized calculations with the TREDI code. Note that the results obtained by both codes are very similar.

With those initial undulator parameters and the plane wave approximation, we run 1-D simulations varying the THz power and the undulator length. The results show that with 1MW THz power (intensity ~6MW/cm^2), and the undulator length L_u of 40 cm, the original electron beam is bunched into a series microbunches with 50% particles contained in the ~50μm bunch length (FWHM) of after 1 m ballistic drifting.
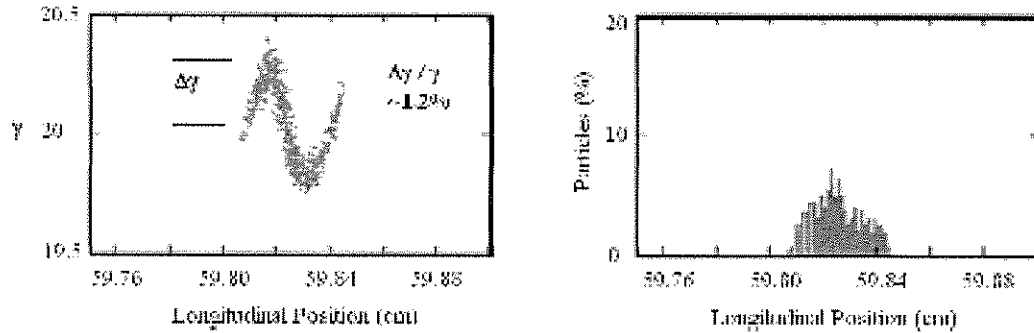
Figure 3.3: Phase space distribution and histogram of electrons in one THz wavelength at the end of the 40cm-long IFEL undulator (TREDI)
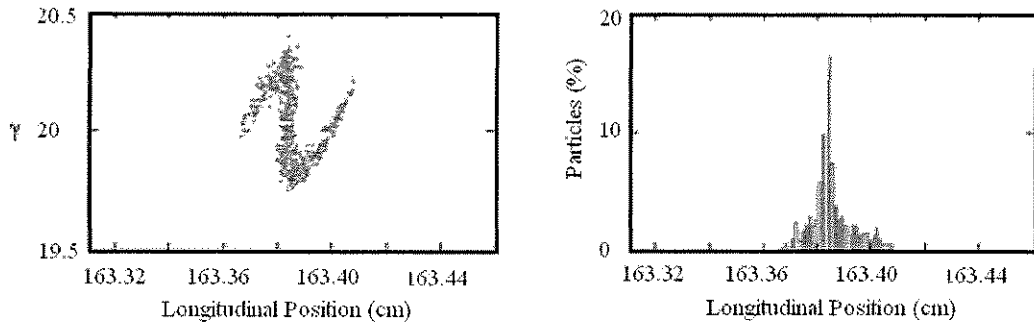
Figure 3.4: Phase space distribution and histogram of electrons in one THz wavelength at 1 meter after the 40cm-long IFEL undulator (TREDI)

For 3-D *TREDI* simulations, we used the same parameters and for the numerical convergence purpose, the electron beam is set to propagate 20 cm in a free space before entering the undulator. Fig. 3.3 and 3.4 show the phase space distribution of electrons within one THz wavelength (left) and its histogram (right) at two different positions. As seen in Fig. 3.3, at the end of a 40 cm-long IFEL undulator (longitudinal position z = 60cm), the phase space distribution shows the sinusoidal-like energy modulation of the electron beam and the maximum energy modulation ($\Delta\gamma/\gamma$) is around ~1.2% (as seen in Fig. 3.3). After drifting in the free space for 1 m, faster electrons catch up with slower ones and microbunching is optimal (Fig. 3.4).

From the histogram in Fig. 3.4, we deduce that the bunch length of 50 μm (containing 50% trapped particles) is obtained at the optimal drifting distance of 1m. Note that according to simulations the bunch length ~50μm can be preserved with negligible debunching for over 1 m. This large value of the acceptance length is important for future applications. The undulator, THz parameters and the optimal bunching results are summarized in Table 2. The electron beam parameters we used in simulations are

23

corresponding to that of the Neptune Photoinjector [24]. The simulation results show that the easy-to-build undulator produced the desired bunch length and amount of trapped particles after a reasonable bunching distance.

THz radiation power	~ 1 MW ($I_{peak} = \sim 6$ MW/cm^2)
Injection e$^-$ energy	10 MeV (0.25% energy spread)
Undulator length	40 cm
Undulator wavelength	5 cm
Permanent magnet	0.658 T
K factor	3
Bunch length	**50 μm**
Trapped particles	**50%**
Drifting distance for optimal bunching	**1 m**

Table 2: Input and output parameters for the optimal bunching case of TREDI

It is interesting that, as shown in [25], the same undulator design can be used to bunch electrons on higher harmonics of the resonant frequency. Therefore, in our case, we can study microbunching of electrons for a plasma density $\sim 10^{17}$ cm^{-3} ($\lambda_p = 114$ μm)

3.3 3-D FEL simulation code *GENESIS 1.3* and microbunching results

We have already seen that a set of undulator parameters that work for an IFEL can also work for a FEL due to the same resonant condition. However, for the FEL microbunching we would like to place emphasis more on the tunability comparing to that in IFEL microbunching because it is more practical to tune the wavelength of the THz seed source because a relatively low seed power of around ~kW is sufficient. The tunability of the seeded FEL microbunching can be achieved by injecting a seed pulse with different wavelengths and an electron beam with energy γ matching the FEL resonance condition. A seed source based on DFG in a GaAs crystal can generate radiation in the range of 0.5-3 THz [26,27]. Therefore, instead of using the undulator parameters from the previous section, we optimized the undulator parameters taking into account change of the electron beam energy from $\gamma=15$ to $\gamma=26$.

E-beam Parameters	Energy	Bunch length	Beam size	Current	Transverse emittance
	8-14 MeV	~10 ps FWHM	~ 200 μm	20-80 A	5-15 mm-mrad

Table 3:   Electron beam parameters for FEL simulations

Here we consider driving an FEL amplifier with an electron beam from a RF photoinjector (typical electron beam parameters are shown in Table 3) and amplifying the frequencies provided by the seed source. The resonant condition (red solid curve in Fig. 3.5) is chosen for the study such that γ~26 and 15 correspond to $\lambda=100$ μm and 300 μm, respectively.
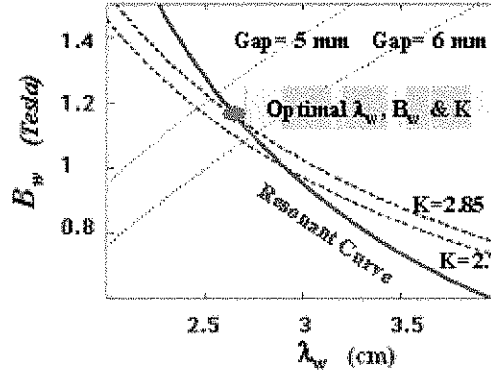
Figure 3.5: Optimization of the waveguide FEL amplifier tunable in 0.5-3 THz range

After obtaining the resonant curve, we can use a similar method described in the previous section to optimize other important parameters (such as λ_w, B_w, and gap between the faces of the magnets, as shown in Fig. 3.5). λ_w and B_w are chosen to give reasonable values of K (dashed curves in Fig. 3.5) to maximize the FEL interaction along the resonant curve of given γ and λ within the Halbach criterion (dotted curves). On the other hand, a circular waveguide with a size smaller than the gap between the pole pieces of the magnet is chosen such that the propagating mode size can cover the whole wiggling electron beam.

After several iterations in choosing the undulator parameters, the optical waveguide ID is 5 mm and a planar undulator with λ_u=2.7 cm, and B_u=1.14 T (K=2.85) is chosen for the following simulations. Note that the fundamental mode size (1/e radius of the mode amplitude) of the THz radiation inside the waveguide is around 1.5 mm. It covers the whole wiggling motion amplitude (< 700 µm) plus the electron beam transverse size (~ 220 µm.).

26

A three-dimensional, time-dependent simulation code, *GENESIS 1.3* is used for modeling the FEL amplification and microbunching process as in the waveguide. *GENESIS 1.3* solves a set of self-consistent differential equations based on Maxwell's and Hamilton's equations that describe the physics of an FEL, including the space charge effect [11]. In the simulations, we co-propagate a 10ps FWHM electron bunch and a continuous THz seed pulse in a simulation box with a cross-section of 5mm x 5mm to model the conditions for a waveguide FEL microbuncher.

3.3.1 FEL microbunching results

The simulation results of microbunching electrons in a waveguide THz FEL are shown in Fig. 3.6. Here a 1kW power seed radiation with a wavelength of 200 μm and an electron beam with a peak current 60 A and $\gamma = 19.5$ are used. In a high gain seeded FEL, the seed radiation modulates the electron beam slightly and the modulated electron beam radiates coherently to further amplify the radiation. This positive feedback leads to stronger bunching of the electron beam and thus an even higher radiation power. As a result, an exponential gain of the THz power, as shown in Fig. 3.5(a), is expected. Snapshots of the phase space distribution of electrons along the FEL undulator shown at z= 0.5m (b), 1.5m (c), 1.8m (d) and 2.5m (e).
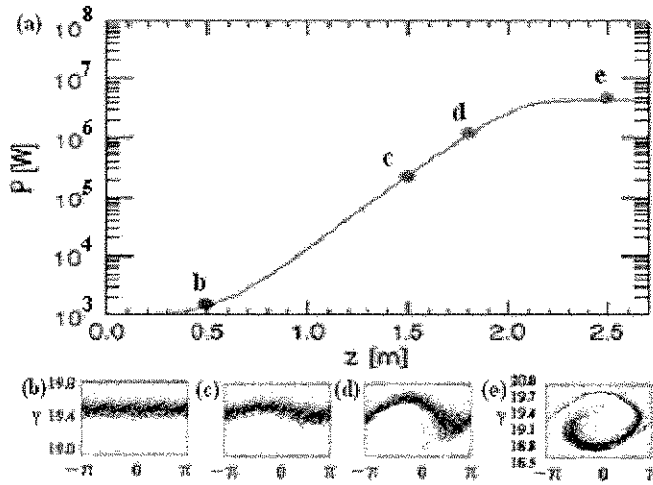
Figure 3.6: THz power as a function of the undulator length z (a) and the phase distribution of electrons in one radiation wavelength at (b) 0.5m (c) 1.5m (d) 1.8m, and (e) 2.5m. (Seed power= 1 kW, peak current =60 A, γ= 19.5, and λ =200 μm)

In terms of microbunching, the stage that we are most interested in occurs at 1.8m (corresponding phase space distribution is in Fig. 3.6(d)) where the energy modulation is optimal at ~ 1.3% and phase space folding is yet to occur. The electron beam with such magnitude of the energy modulation will be microbunched with ~50% particles contained in bunches that are ~ λ/6 FWHM long. In order to transfer the energy modulation to the current modulation, ballistic drifting of the beam over a distance of 1 meter or using a chicane (magnetic dispersive device) is required.

3.3.2 Inhomogeneous microbunching in FEL due to slippage effect

When a long FEL is driven by a short electron pulse, such as that produced by a photoinjector, the number of periods of the wave covering the electron bunch is smaller than the number of wiggler periods. The radiation eventually outruns the whole electron

28

beam and amplification process is terminated because of the slippage. This effect is stronger when operating at a longer wavelength thus limiting the overall gain of the FEL amplifier. The longitudinal structure within an electron beam also becomes rather complicated due to this slippage effect.

One such example is shown in Fig. 3.7, where a 10-ps electron beam is interacting with a 300-μm radiation in a 1.8-m long undulator with a period of 2.7 cm. As seen in Fig. 3.7, for phase space distribution of electrons at z = 1.8 m, the energy modulation is different for different slices of the macro-electron pulse. Notes that the width of the slice is equal to the seed radiation wavelength of 300 μm.
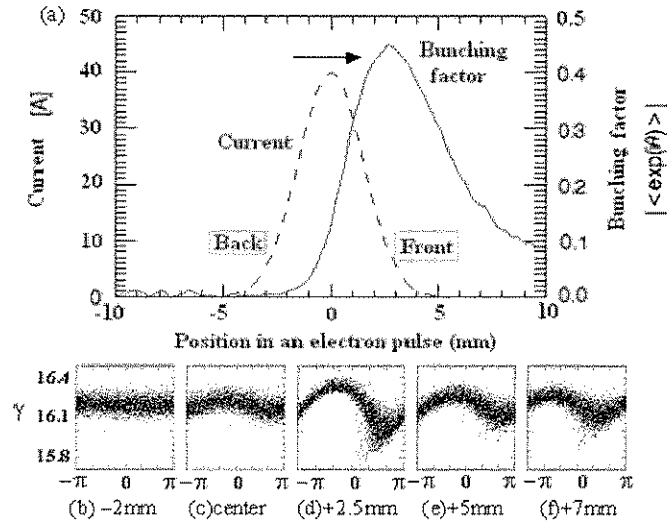
Figure 3.7: Bunching factor (a) and phase space distribution at different slices (b,c,d,e,f) of the 10-ps FWHM electron pulse propagating 1.8 m inside the undulator. The arrow shows the propagation direction of the electron beam. Seed power is 1 kW, peak current is 40 A, γ = 16.2, and λ= 300 μm.

Because the newly emitted radiation always overtakes the electrons that generate it,

electrons constantly "see" the radiation amplified by other electrons behind them. Therefore, the energy modulation is stronger for the electrons slightly in front of the center of the Gaussian pulse. This phenomenon results in inhomogeneous modulation of the electron beam. The bunching factor $F = \left| \left\langle e^{i\theta} \right\rangle \right|$, where θ is the phase at which each electron is located inside a period of a THz wave, is proportional to the ratio of the bunch length and the separation between bunches. F peaks at ~ 0.45 for electrons on the front of the electron pulse and indicates inhomogeneous microbunching (Fig. 3.7 (a)).

It is important to study the longitudinal dynamics of electron beam modulation imprinted via FEL interactions in the undulator. It may be possible to obtain a more uniform microbunching by shaping the electron beam such that the current distribution is asymmetric with a slow rise time and a rapid fall rather than a Gaussian distribution. Such a ramped beam was recently obtained in the Neptune Laboratory [23]

Note that with a peak current of 40 A and the THz wavelength of 300 μm, the energy modulation of the electron beam $\Delta\gamma/\gamma$ has a maximum of $\sim 1.25\%$ after propagating 1.8 m inside the undulator (Fig. 3.7 (d)). This result is comparable to the result with a peak current of 60 A and the THz wavelength of 200 μm (Fig. 3.6 (d)). It means that for any given undulator length, microbunching is not only tunable but also can be optimized by scanning the peak current at each wavelength.

3.4 Summary of THz IFEL and FEL microbunching in Neptune Lab

In previous sections, we presented the simulation results for THz IFEL and FEL microbunching using parameters feasible in experiments at the Neptune Lab. According to numerical modeling shown in Sec 3.2 and 3.3, both IFEL and FEL techniques can be used to modulate the energy of a relativistic electron beam on the THz scale. Simulation results in both cases show that with straightforward planar undulator and electron beam parameters, ~50% particles can be bunched within ~ $\lambda/6$ (FWHM) in the THz range after ballistic drifting in 1-2 meter. The THz IFEL and FEL microbunching schemes are concluded in Fig. 3.8.
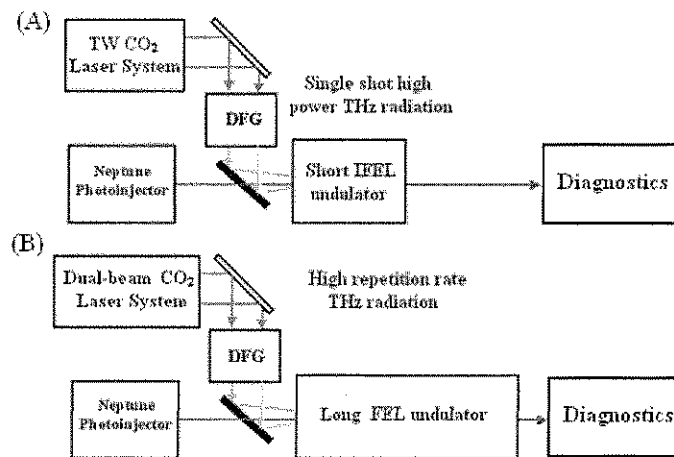
Figure 3.8: Schematics of THz (A) IFEL and (B) FEL microbunching experiments at Neptune Lab, UCLA

Both IFEL and FEL microbunching experiments contain 3 parts: a radiation seed source, an undulator, and diagnostics. The main difference between IFEL and FEL microbunching is the requirement on the THz seed power level. As a result of a less powerful THz seed in FEL, the undulator length needed for FEL microbunching is much

longer.

The THz seed may be produced by difference frequency generation in a GaAs nonlinear crystal pumped by two lines of a CO_2 laser. Such a seed is not only relatively narrow band but it is also phase-locked to the CO_2 beat-wave that generates it. According to simulations, IFEL microbunching requires roughly a MW power THz radiation that can be produced in a single-shot experiment [27]. On the contrary, the THz FEL microbunching only requires a ~ 1kW seed pulse which could generated using commercial CO_2 lasers running at 1 Hz [26]. In Chapter 5, we will present experimental results on development of both types of seed sources.

When FEL is driven by a photoinjector-based short electron beam, the slippage effect due to velocity mismatch between the amplified radiation and the electron beam can cause longitudinally inhomogeneous microbunching. Note that on a THz scale, this longitudinal dynamics of a modulated beam is still possible to measure directly using a sub-picosecond streak camera or other diagnostic techniques [23]

Since a bunched electron beam can emit coherent radiation on the scale of the bunch length, another important application of the seeded FEL mechanism is amplification of the THz radiation pulses to a very high power. The radiation aspect of FEL in the THz range will be examined in the next chapter.

4. Seeded FEL techniques for THz radiation amplification

Free-Electron Laser interactions can be used to modulate the electron beam longitudinally and to generate high-output power radiation in the THz frequency range. The THz range of the electromagnetic spectrum can be conveniently covered by FELs because the electron beam parameters needed are relatively easily realized using current technology. Three FEL operations can provide THz pulses: an FEL oscillator, a Self-Amplified Spontaneous Emission (SASE) FEL and a seeded FEL amplifier. In the first case, a multi-pass FEL oscillator is driven by a few microsecond long electron beam. The low peak current in the beam and losses attributed with the cavity optics make the task of obtaining high THz peak power difficult. A SASE FEL is capable of producing MW power THz pulses in a very long (~ 6-10 m) undulator [28]. However, the radiation pulse in a SASE FEL is built up from spontaneous noise, which makes synchronization with an external event or a laser pulse on a sub-picosecond time scale extremely difficult, and the radiation pulse is typically not phase coherent over its entire duration. An external EM wave seed in a single-pass FEL amplifier can not only solve the synchronization issue but also improve the coherent properties of the radiation. Most importantly, it significantly shortens the undulator length, thus opening the possibility of driving FELs with a short, high peak current beam and reach a very high FEL gain. Recently, there is a growing interest in seeding FELs in the visible and X-ray range [29-38]. However, in the THz range this technique is not studied yet due to the lack of a suitable radiation seed source.

At the Neptune laboratory at UCLA we have launched an experimental program towards development of a THz radiation source that can act as a seed for the single-pass

33

FEL amplifier. As will be shown in the next chapter, a tunable seed source is being built and characterized. These developments have stimulated detailed analysis of a seeded THz FEL driven by a high-peak current photoinjector, which we present below.

In this chapter we analyze two seeded FEL techniques from the point of view of production of multi-megawatt radiation pulses on the THz scale: High-gain FEL amplifier, and High-Gain Harmonic Generation (HGHG) FEL. The time-dependent FEL code *Genesis 1.3* is used for analysis.

In Section 4.1, we first consider a high-gain FEL amplifier, where a kW seed pulse generated via DFG in the 0.5-3 THz range is amplified in a waveguide to tens of MW. DFG in a GaAs crystal cannot produce seed pulses with reasonable efficiency at frequencies higher than 3 THz due to the strong phonon absorption in the material. To extend the THz FEL output spectrum above 3 THz, we consider lasing on the third harmonic of the seed radiation using HGHG. This method has been successfully demonstrated in the visible and UV ranges [39]. In Section 4.2, we then discuss a THz HGHG FEL, where a short modulator seeded by a MW power pulse in the 0.5-3 THz range first bunches the beam and is followed by a second radiator-undulator tuned to the third harmonic (1.5-9 THz) of the fundamental frequency. Using this technique, the HGHG allows extending the spectral range of high-power radiation to 3-9 THz.

4.1 Simulations on high-gain seeded THz FEL amplification

4.1.1 Parameter space for FEL amplifier modeling

It is known that power increase in a high-gain, seeded FEL is directly related to the microbunching process occurring along the undulator. As described in Section 2.3, FEL amplification proceeds in three stages. Stage one is so called linear stage where electrons gradually get modulated at the entrance of the undulator, and the EM-wave grows slowly. Stage two is the exponential growth section where modulated electrons radiate coherently to amplify the radiation. The third, saturation, stage occurs when electrons are trapped in the ponderomotive wave and the energy lost by electrons is balanced by the energy gained from the wave. In this section, we would like to focus on the gain and the saturation level of the FEL amplification.

E-beam				THz radiation		Undulator	
Energy	8-14 MeV	Beam size	100-250 μm	Wavelength	100-300 μm	Period	2.7 cm
Current	20-60 A	Length	~10 ps	Seed power	~ 1 kW	K	2.85(1.14 T)
Transverse emittance		5-15 mm-mrad		Length	~ 200 ns	Gap	5.5 mm

Table 4: Parameters for waveguide FEL microbunching using *GENESIS* 1.3

Taking into account the parameters achievable at the Neptune Laboratory, we use the same undulator parameters as described in Section 3.3. Note that with the undulator with a fixed gap and an optimal K value, the tunability of the seeded FEL microbunching can be achieved by injecting a seed pulse with different wavelengths and an electron beam with

energy γ matching the FEL resonance condition. The parameters for simulations are summarized in Table 4.

A three-dimensional, time-dependent simulation code *Genesis 1.3* is used for modeling the FEL amplification process in the waveguide.

4.1.2 Simulation results on tunable THz FEL amplifier

In the simulations, we co-propagate a 10ps FWHM electron pulse and a continuous THz pulse in a simulation box with a cross-section of 5mm x 5mm to model the conditions for a waveguide FEL amplifier. With the electron beam and undulator parameters given in Table 4, we vary the peak current of electron beam and the THz seed power in order to study the amplification of the radiation pulse. The results are shown in Fig. 4.1. Note that electron beam energy γ is tuned to fulfill the resonant condition for a waveguide FEL (e.g. $\gamma = 19.5$ for 200 μm radiation instead of $\gamma = 18.4$ in a free space) due to the phase velocity increase (longer λ_{eff}) inside the metal waveguide.

As seen in Fig. 4.1(a), with a fixed beam current 60 A, a higher seed power does not significantly affect either the gain length or the saturation power level but only makes the saturation happen slightly earlier. It shows that the tolerance of the process to variations in the seed THz power is high and a ~1 kW seed pulse can be amplified to more than 4MW in ~2 meters for a relatively modest peak current of 60A.

36
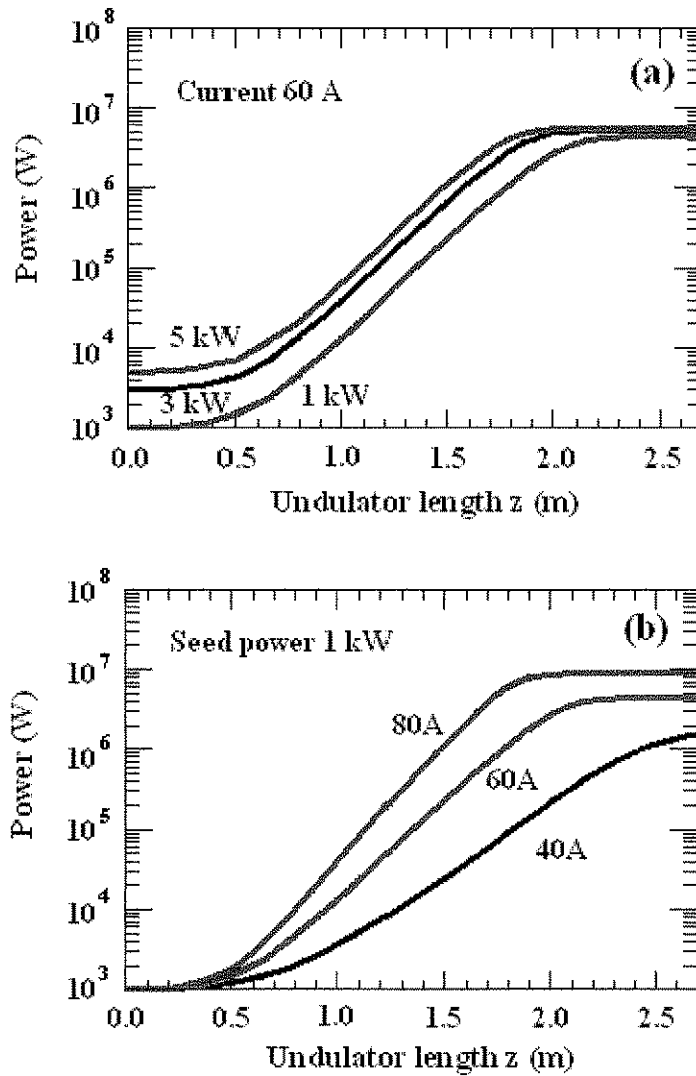
Figure 4.1: Calculated THz power as a function of the undulator length z
(a) for a fixed peak current of 60 A and variable seed power level and
(b) for a fixed seed power of 1 kW and variable peak current of the electron beam
(Energy of the electron beam $\gamma = 19.5$, and $\lambda = 200$ μm)

The electron beam peak current is a critical factor for the saturation power and the

gain in a FEL. As shown in Fig. 4.1(b), for a fixed seed power of 1 kW, when the peak

current increases from 40 A to 80 A, the gain length (the distance for which the radiation

field is amplified by a factor of e), decreases from 45 to 25 cm and the saturation power increases from 1.5 MW to ~10 MW. A higher gain for a higher peak current causes the saturation to happen over a shorter undulator length. This modeling indicates that it may be possible to reach very high peak powers on the order 100 MW for THz pulse in a relatively short (few meter long) FEL undulator. For this, an electron pulse with a peak current of ~100 A in combination with slight tapering of the undulator for the last few periods is required. A preliminary simulation result is shown in Fig 4.2.
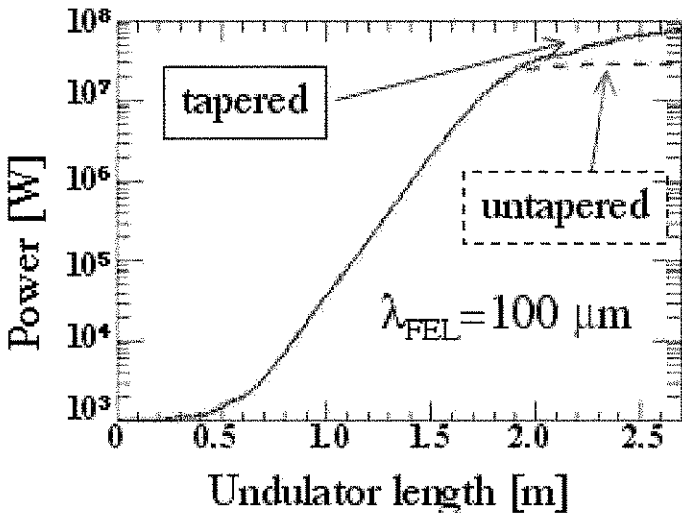
Figure 4.2 Calculated power in 100 μm FEL amplifier as a function of the undulator length for a peak current of 100A with tapering (solid line) and without tapering (dashed line).

In Fig. 4.2 the linear tapering of the undulator's gap was applied from ~ 1.5 m of propagation of a 100 μm pulse in the undulator. At 1.9 meters both tapered (solid line) and untapered (dashed line) scenarios result in a power of 20 MW. Then the untapered

undulator stops amplifying the pulse, but in the 2.5 m long tapered undulator the peak

power reaches 75 MW. The deviation from exponential growth in power and a relatively

small power enhancement for the tapered undulator is attributed to the fact that the

saturation mechanism is dominated in this case by the slippage effect between the electron

beam and the amplified THz radiation as described in Sec 3.3.2. When number of periods

of the THz wave covering the electron bunch is smaller than number of wiggler periods,

the radiation eventually overtakes the whole electron beam and stops being amplified

because of the slippage. This effect is stronger when operating at a longer wavelength and

the wavelength dependence of the saturation level can be seen more clearly below.
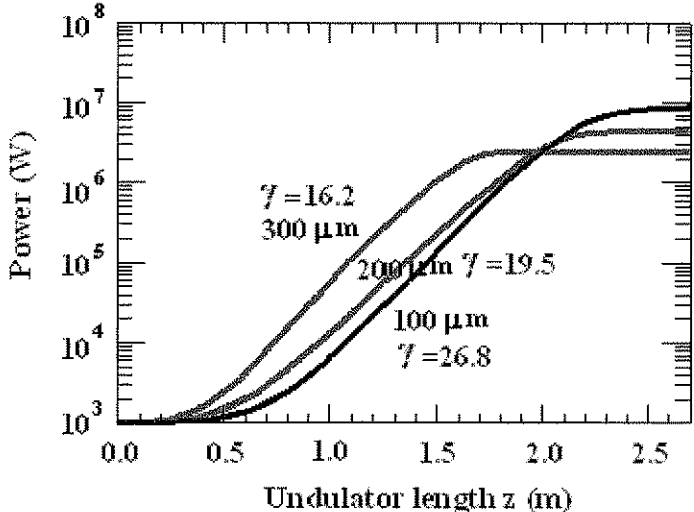
**Figure 4.3: Calculated THz power as a function of the undulator length z for a fixed
peak current of 60 A and different wavelengths**

Spectral tunability of the optimized undulator is shown in Fig. 4.3. The tunability of

the seeded FEL amplifier can be achieved by injecting a seed pulse with different

wavelengths and an electron beam with γ matched for the resonance. Simulations were run to model three fixed wavelengths 100, 200, and 300 μm. However, full coverage of the spectral range of 0.5-3 THz is expected. Note that in Fig. 4.3, the gain (slope) differences between various wavelengths are mainly due to the electron energy, and the saturation power levels depends upon the effect of slippage. As expected, with a longer electron beam, the saturation power will be higher and reached later.

In summary, the simulation results show it is feasible to amplify a kW seed pulse in the 0.5-3 THz range to tens of MW with a high-gain FEL amplifier and modest electron beam parameters. We can further extend the spectral range of high-power radiation to 3-9 THz where the needed seed pulse is not easily generated in nonlinear crystals, if we apply the HGHG technique discussed in the next section.

4.2 Simulations on high-gain harmonic THz generation

In HGHG FEL, an electron beam prebunched by the fundamental radiation in the first planar undulator (prebuncher) also carries perturbations at the higher harmonics; therefore, when the prebunched beam is sent into a second undulator (radiator) designed only to resonate with the third harmonic for FEL emission, the third harmonic becomes the new fundamental in the radiator and can have a very high gain. Besides its potential to expand the frequency range of the high power THz sources, the stand-alone prebuncher itself allows studying of saturated FEL microbunching at the 0.5-3 THz scale.
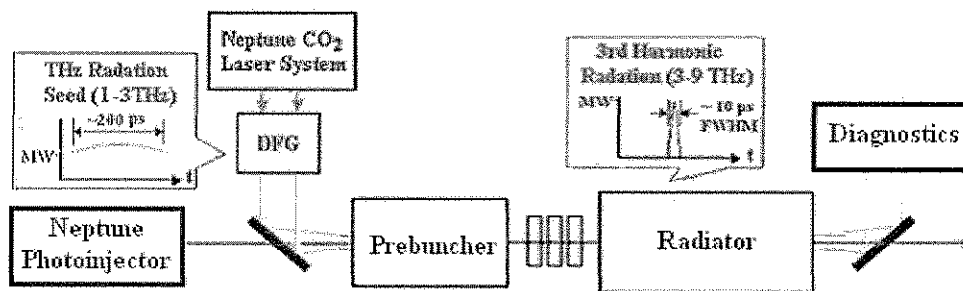
Figure 4.4. Schematic of the high-gain harmonic generation arrangement

The schematic of the HGHG experiment using the 2-m long undulator is shown in Fig. 4.4. We consider using a ~MW peak power THz seed pulse, generated by the Neptune TW CO_2 laser system via DFG, to modulate the electron beam energy in a 30-cm long FEL prebuncher. After ballistic drifting, the energy-modulated electron pulse becomes a current-modulated pulse and is injected into the third harmonic radiator. A magnetic triplet is used to match the e-beam spot sizes between the two undulators.

41

The undulator parameters for the short prebuncher are the same as those of the FEL undulator that was described in the previous section due to the identical resonant condition. As for the HGHG radiator, K factor needs to be decreased to 1.17 from 2.85, according to Eq. 2.3, to fulfill the resonant condition for the third harmonic of the THz seed. This in practice can be done by increasing the gap between magnets of the long FEL undulator optimized in the section 4.1.1.

4.2.1 Saturated FEL microbunching and harmonic modulation

If the power of a seed pulse is far greater than the FEL saturation level, i.e. 10-100 MW for a 60 A electron beam (seen in Fig. 4.3), then energy is transferred from the radiation to electrons via an IFEL mechanism [20]. The IFEL in the THz range can provide more homogeneous microbunching of a relativistic electron beam in a short undulator [7,40] compared to an FEL. However, the 10s of MW level of THz power needed is rather difficult but not impossible to obtain. Here we consider microbunching in a highly saturated FEL regime, where the power level of few MW is close to saturation but not above it, and strong FEL interactions take place immediately after injection of an electron beam in the undulator. This allows using a short undulator for THz bunching where the slippage effect is not yet critical.
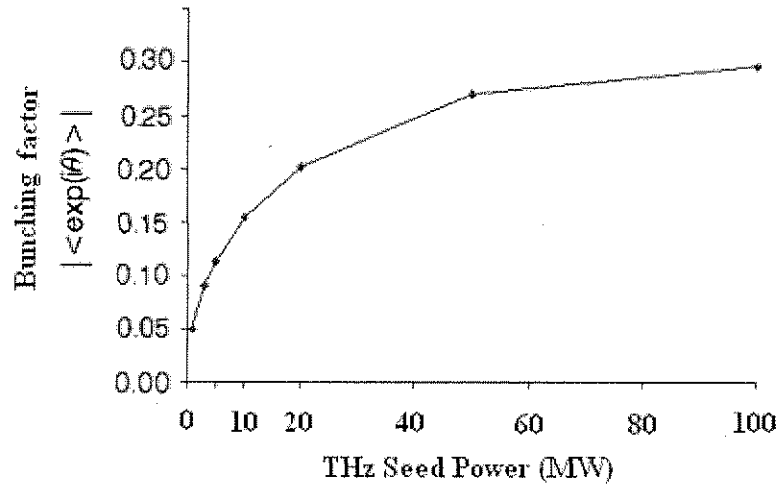
Figure 4.5: Bunching factor of an electron beam after propagating in a 30 cm long, K=2.85 prebuncher seeded with various power of 100 μm pulses

For the undulator parameters used in the previous session, we study the dependence of bunching factor versus the seed power at the exit of a 30 cm long undulator. It is presented in Fig. 4.5. In the simulations, the starting level of the seed power is 1 MW, where the deviation of THz power from the exponential region on the gain curve in Fig. 4.3 begins. As seen in Fig. 4.5, the bunching factor grows with an increase in the seed power level; however, the bunching factor F (as explained in Sect. 3.3.2) is saturated at ~0.3 at approximately 50 MW of power due to the trapping of electrons in the ponderomotive well even with a short undulator.

An electron beam with a linear energy modulation can be compressed using dispersive devices, such as a chicane, to obtain a high peak current in a microbunch. As a result, an energy modulated electron beam before it is trapped is optimal for microbunching. From the simulations we conclude that for optimal microbunching, a seed power in the range of 1-10 MW is desirable, where the electron beam modulation is linear

and FEL interactions occur in a highly saturated regime. Note that this power range is experimentally achievable and it will be discussed in Sec 6.2.

Microbunching in this highly saturated FEL regime for different wavelengths is shown in Fig. 4.6. The bunching factor of an electron beam co-propagating with a 3 MW THz pulse increases along the undulator. When seeded with a longer wavelength radiation, the bunching factor increases faster due to a smaller resonant value of γ. The energy modulation of the electron beam $\Delta\gamma/\gamma$ at the exit of the undulator is $\sim 0.5\%$.
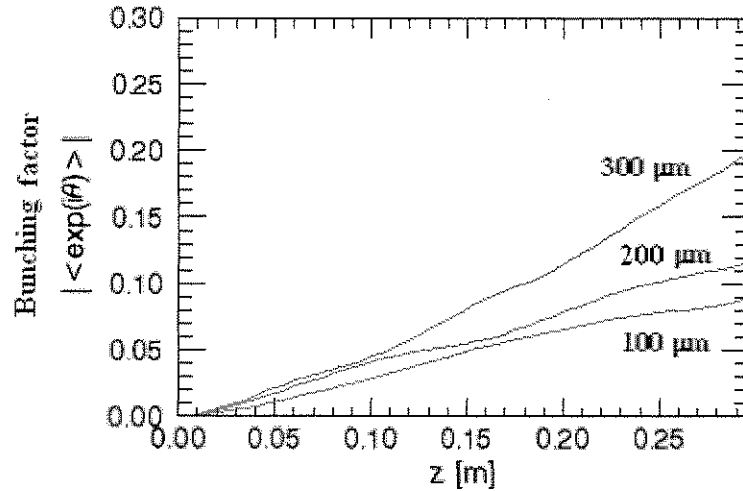
Figure 4.6: Bunching factor of an electron beam co-propagating with a 3 MW seed pulse with various wavelengths 100, 200, and 300 μm in a 30 cm long undulator

The bunching factor along the electron pulse in the saturated FEL regime can be seen in Fig. 4.7. For the same MW level of power for a seed pulse, bunching of the electron beam after the 30 cm long undulator is constant for all temporal slices as opposed to the longitudinal inhomogeneity observed for typical FEL microbunching driven by a short

Gaussian electron pulse (see Fig. 3.6). Fig. 4.7 also shows that the energy modulation in a

planar undulator has the third harmonic component and the bunching factor of the third

harmonic is approximately one order of magnitude less than that of the fundamental.
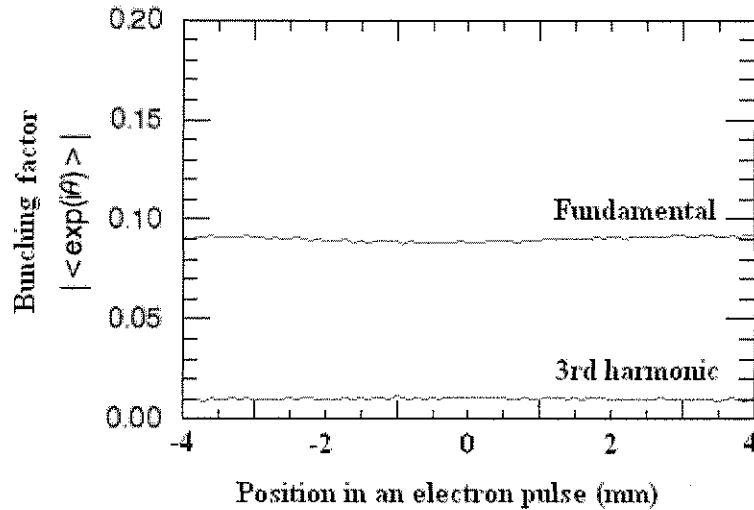
Figure 4.7: Bunching factor of the fundamental and the 3rd harmonic along a
Gaussian electron pulse after 30 cm saturated FEL interaction inside the K=2.85
undulator with a 3 MW seed of wavelength 100 μm

The fact that we observe not only microbunching at the fundamental but also for the

3-rd harmonic suggests that an undulator seeded by the prebunched electron beam can be

used for HGHG seeding. Simulations of this scheme is analyzed in Sec. 4.2.2

4.2.2 THz HGHG FEL simulation results

The *GENESIS 1.3* code was used to model the whole HGHG process including the

saturated FEL prebunching, drifting/beam size matching, and the FEL amplification. A

10-ps long electron beam with a peak current of 60 A is injected into the prebuncher along

with a 200-ps long THz seed pulse with peak power of 3 MW. As was shown in Fig. 4.7, this level of seed power produces homogeneous energy modulation for the entire electron bunch in a short, 30 cm long undulator.
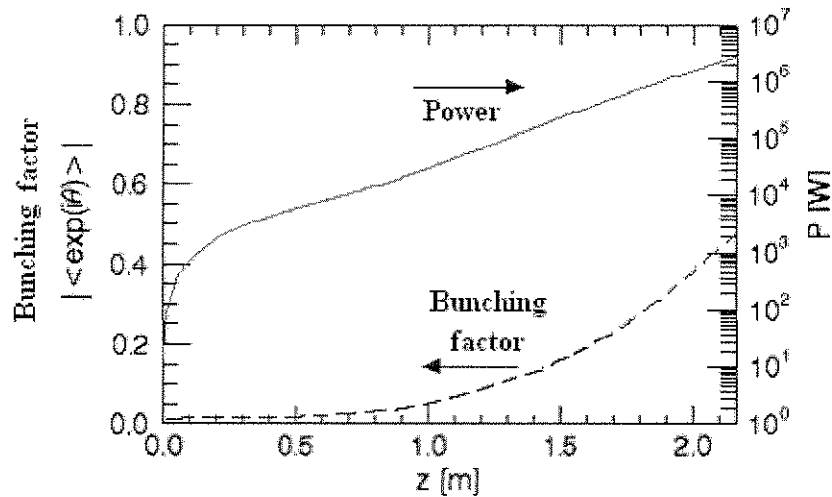
Figure 4.8: Bunching factor and THz power on the 3rd harmonic inside the HGHG radiator after injecting a prebunched electron beam with a peak current of 60 A. The electron beam is prebunched by interacting with a 3 THz pulse with a peak power of 3 MW in a 30 long prebuncher followed by ballistic drifting of 60 cm

After drifting for a total distance of ~60 cm and passing a magnetic triplet, the electron beam has a matched spot size of 350 μm and is injected into the FEL amplifier for HGHG. Due to the energy modulation in the prebuncher and the subsequent current bunching in the drift space, the bunching factor of the third harmonic is 4 orders of magnitude higher in comparison with that of a non-bunched electron beam. This strong current modulation shortens the length needed for building up the undulator radiation inside the FEL radiator. In Fig. 4.8, the bunching factor and power of the third harmonic in

the radiator are presented.

By using a 3 THz pulse with a peak power 3 MW for prebunching of the electron beam, up to ~ 3 MW of power at 9 THz can be generated in a 216 cm long FEL radiator (solid curve in Fig. 4.9) resulting in the 100% conversion efficiency. As a comparison, less than 10 W can be obtained for SASE FEL with the same undulator. Slightly higher beam current can easily result in the power larger than 3 MW for a 2-m long undulator considered for the seeded THz FEL.

We also compared the third harmonic output power while varying the power of the fundamental radiation used to prebunch the electron beam (Fig. 4.9). Fig. 4.9 shows that with more than 1MW seed power and a fixed drifting distance of 60 cm, the power of the third harmonic generation is always reaching MW level in a 2 m long radiator. However, a higher seed power does not assure a higher power of the third harmonic radiation. This happens because electrons are slightly trapped instead of being sinusoidally modulated in the prebuncher when the seed radiation is too strong. Therefore, abruptly bunched electrons build up the third harmonic radiation faster at the beginning of the radiator but eventually their complicated phase space distribution hinders the gain of high harmonic generation in a longer radiator. As a result of this dynamics, there is an optimal THz seed power for prebunching electrons due to the preferable sinusoidal bunching condition at the entrance of the radiator of a given length. As is apparent in Fig. 12, for a 2 m long radiator, a 3 MW seed at 3 THz can generate ~ 2 MW in the third harmonic; however, using 1 MW or 10 MW seems to either underbunch or overbunch electrons in the prebuncher such that the harmonic generation in the radiator is actually reduced.
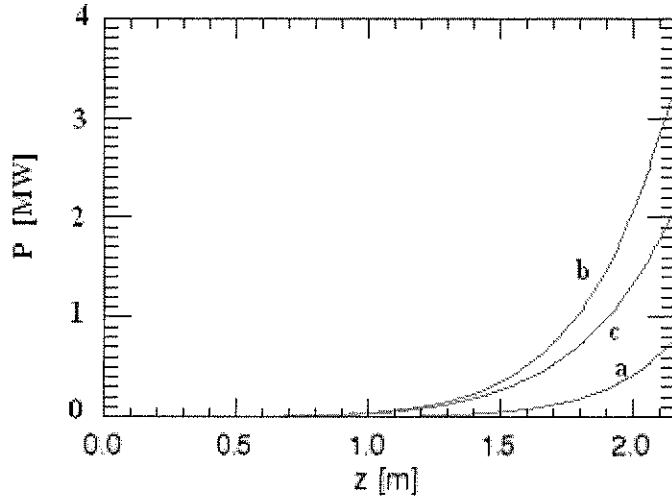
Figure 4.9 3rd **harmonic output power vs the FEL radiator length**
with various power (a): 1 MW (b): 3 MW, (c): 10 MW
of the seed pulse of wavelength 100 μm in the prebuncher

We summarize parameters and simulation results for the HGHG FEL tunable in the range of 3-9 THz are given in Table 5.

		HGHG	
		Prebuncher	Radiator
Undulator Parameters	Period	2.7 cm	
	K	2.85	1.17
	Length	30 cm	2m
THz Seed Parameters	Wavelength	100-300 μm (1-3 THz)	
	Seed power	1-10 MW	
Output THz wavelength		33-100 μm (3 – 9THz)	
Output THz power		> 1MW	
Output THz pulse length		~ 10 ps FWHM	

Table 5:   Parameters of the THz HGHG FEL

48

4.3 Summary of THz FEL

In this chapter, by using 3-D simulation code *GENESIS 1.3*, we demonstrated that FEL amplification is a very efficient way to generate a high power, narrow band radiation in the THz range. We found that a 2 m long FEL amplifier driven by a 10 ps long electron beam with a peak current of 60 A is enough to amplify a seed pulse with the power of ~kW in the 0.5-3 THz range to the power level of ~MW. A tunable, narrowband 1-10MW THz source that is capable of producing electric field E~ 1MV/cm in a focused beam with spot size w_0=600 μm and appear feasible for high-field studies in this unexplored range of spectrum. Note that the most powerful narrowband ($\Delta v/v$ <10%) THz radiation source in this spectral range is an ~1MW FEL at FELIX, Netherlands[12]. A much more compact THz radiation source with ~MW level is of great interest to the community. The high-gain FEL amplifier is capable of producing a record power up to 100 MW by using tapering and an electron beam with a higher current around 100A (2 nC in 20ps).

Another advantage of using a FEL as a high-power (~MW) radiation source in the THz range is the possibility of extending the spectral range to 3-9 THz via HGHG. Due to the phonon band in nonlinear crystals, this spectral range is not accessible using DFG. With HGHG at long wavelength scale, we can also study the dynamics of high harmonic microbunching in a FEL, which is an interesting topic in Beam Physics.

49

5. Development of THz radiation sources

As was shown in the previous chapter, seeding of an IFEL/FEL requires a narrow-band ($\Delta v < 50 GHz$), high power (kW to MW) source tunable in the terahertz (THz) frequency range between 300 GHz - 3 THz (wavelength 1000-100 μm). There are considerable problems in developing practical high-power sources of coherent radiation that are tunable in this range. Electronic techniques in the microwave range are difficult to extend beyond 200 GHz; on the other hand, optical techniques of quantum electronics are difficult to extend below 10 THz. Besides being necessary for seeding FELs such a source once developed, would be useful for spectrally selective analysis of biomedical and semiconductor samples, or monochromatic THz imaging.

Frequency down-conversion of the nanosecond lasers in nonlinear crystals is proven to be the most successful techniques for generating narrow-band, high-power THz pulses. In this chapter, we first in Sec. 5.1 describe the theory of Difference Frequency Generation (DFG) and discuss a crystal choice for DFG in the THz range. Then we discuss experimental results on THz generation via DFG nonlinear mixing of CO_2 laser lines. In Sec. 5.2, we show the development of a high repetition rate tunable seed source with 2 kW of power using a 200-ns pump pulse from a commercial TEA CO_2 laser [41]. In Sec. 5.3, in a single-shot experiment, we demonstrate generation of 1 THz pulses with a peak power up to 2 MW using the multi-gigawatt CO_2 laser pulses in the Neptune Laboratory [27]. According to simulation results from previous chapters, these power levels should be sufficient for the seeded THz FEL/IFEL microbunching.

5.1 Difference Frequency Generation in nonlinear crystal

5.1.1 Theory of difference frequency generation

In order to understand DFG in a nonlinear crystal, we first need to understand the nonlinear frequency-mixing processes.

In the case of conventional (i.e., linear) optics, the induced polarization (dipole moment per unit volume) $P(t)$ depends linearly upon the electric field strength that can often be described by the relationship

$$P(t) = \chi^{(1)} E(t),$$

where the constant of proportionality $\chi^{(1)}$ is known as linear susceptibility.

In nonlinear optics, the nonlinear optical response can be written as a power series in the electrical field strength $E(t)$:

$$P(t) = \chi^{(1)} E(t) + \chi^{(2)} E^2(t) + \chi^{(3)} E^3(t) + \cdots$$
$$\equiv P^{(1)}(t) + P^{(2)}(t) + P^{(3)}(t) + \cdots$$

Here, the coefficients $\chi^{(n)}$ are the n-th order susceptibilities of the medium. For any three-wave mixing process, the second-order term is crucial; it is only nonzero in media that have no inversion symmetry. If we write

$$E(t) = E_1 e^{-i\omega_1 t} + E_2 e^{-i\omega_2 t} + c.c.,$$

where c.c. denotes the complex conjugate (E_1 and E_2 being the incident beams of interest), the second-order term should be

51

$$P^{(2)}(t) = \chi^{(2)}(E_1^2 e^{-2i\omega_1 t} + E_2^2 e^{-2i\omega_1 t} + c.c.)$$
$$+ 2\chi^{(2)}(E_1 E_2 e^{-i(\omega_1 + \omega_2)t} + c.c.)$$
$$+ 2\chi^{(2)}(E_1 E_2^* e^{-i(\omega_1 - \omega_2)t} + c.c.)$$
$$+ 2\chi^{(2)}(E_1 E_1^* + E_2 E_2^*)$$

The frequency mixing process shows how nonlinearities in the response of a material system to an intense laser field can cause the polarization of the medium to develop new frequency components not present in the incident radiation field. Those new frequency components of polarization act as sources of new frequency components of the electromagnetic field.
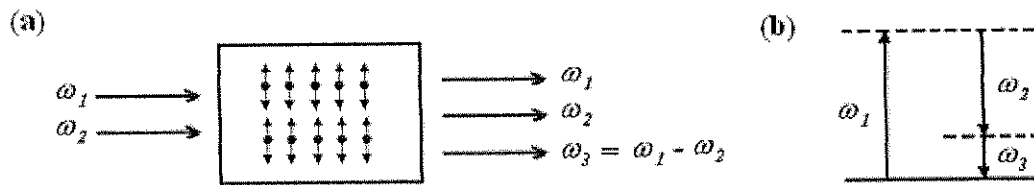
Figure 5.1 (a) Difference frequency generation and (b) energy-level description

Let us now consider the situation of difference frequency generation as shown in Fig. 5.1. Due to nonlinearities in the atomic response (related to the $e^{-i(\omega_1 - \omega_2)t}$ term of $P^{(2)}(t)$), each atom develops an oscillating dipole moment that contains a component at frequency

$$\omega_3 = \omega_1 - \omega_2, \tag{5.1}$$

where ω_1 and ω_2 are input frequencies. Any material sample contains an enormous amount of atomic dipoles, each oscillating with a phase that is determined by the phases of the incident fields. However, under a certain condition, known as the phase matching condition, the system will act as a phased array of dipoles and radiate constructively in the

52

As apparent in the insert of Fig. 5.4, the refraction of the pump and THz beams in a noncollinear configuration allowed the separation of the newborn radiation from the pump lasers in space. The transmitted pump beams were sent to the fast photodetectors to control the timing between two pulses. The THz radiation was collected by an off-axis parabolic mirror and sent onto a Golay cell for detection. The detector with a known spectral response for both the THz and IR wavelengths was calibrated in an energy scale using the 10-μm pulse. The experimental set-up shown in Fig. 5.4 was modified for collinear phase matching simply by placing a 135 gr/mm grating in the plane where the two CO_2 laser beams intersect. The grating worked as a beam combiner and after the grating two collinearly propagating beams were slightly focused by a curved mirror and a beam sent on a GaSe crystal. Two z-cut samples of GaSe with a length of 10 and 12 mm were tested in the experiments.

5.2.2 Results in THz generation using a room temperature GaAs

A semi-insulating crystal of Cr-doped GaAs (specific resistivity ~$4x10^8$ Ωcm) was used in this work. The crystal was cut along a [111] direction so that the input polarization vector was parallel to this direction and the input face was perpendicular to a (111) plane. This orientation has the maximum nonlinear coefficient [47].
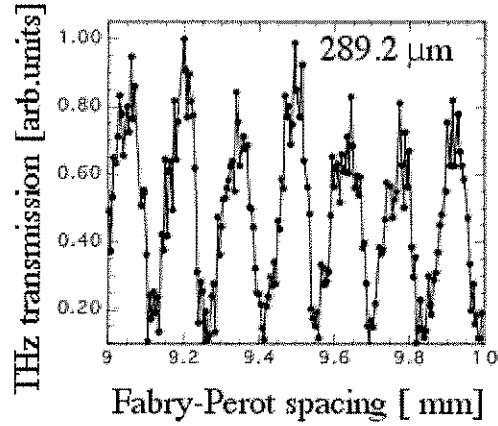
Figure 5.6 The THz signal at 289.2 μm transmitted through the scanning Fabry-Perot interferometer versus the spacing distance varied from 9 to 10 mm

To measure the spectral bandwidth of the THz radiation produced by mixing CO_2 laser lines in GaAs, a high-finesse scanning Fabry-Perot interferometer was built. A pair of wire grid polarizers (G25 model, Microtech Instruments) with a reflectivity for polarized THz beam better than 99.9% was used for this purpose. The coefficient of finesse F for the interferometer was around 3000. We scanned the Fabry-Perot spacing from 1 to 10 mm. No broadening of the full-width at half maximum for the transmission peaks was observed in this range indicating that the bandwidth was dominated by that of the instrument. In Fig. 5.6, for the 289.2 μm line we present the measured transmission through the Fabry-Perot interferometer, when spacing was changed from 9 to 10 mm. One can estimate the minimum resolvable wavelength interval $\Delta\lambda_{min}$ using a formula

$$\Delta\lambda_{min} = \frac{2\lambda}{\pi m \sqrt{F}} \tag{5.5}$$

where λ is the radiation wavelength and m is the interference order[50]. For the spacing

equal to 9.83 mm and the wavelength of 289.2 μm, m=68. Then Eq. 5.5 gives $\Delta\lambda_{min}$ = 0.049 μm. Based on these measurements the bandwidth of the THz radiation was better than 1.7×10^{-4}. Note that the central frequencies of CO_2 laser lines are measured to a very high metrological precision [51] so the difference frequency is known automatically, and this is an advantage of the described narrow-band THz source. There is no need to use an interferometer- a typical tool to measure the THz frequency.

Tunability in the broad range of 0.5-2.8 THz or 600-110 μm was achieved with a very good agreement between the calculated and measured phase matching angles. In Fig. 5.7, we summarize the experimental data on the spectral dependence of the THz power.
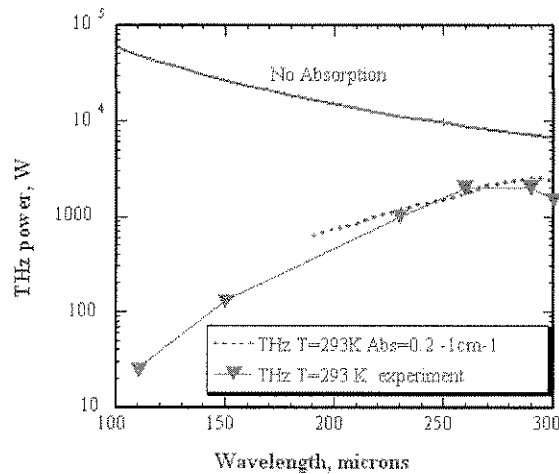
Figure 5.7 Calculated (solid line) and measured (triangles) DFG peak power in the THz range

For the 200 ns pulses with a peak power of $P_{10.3} \approx P_{10.6} \approx 6$ MW in an unfocused laser beam, we detected THz pulses with energy of 400 μJ corresponding to a peak power of 2 kW. The measurement was performed by mixing the 10R(22) and 10P(26) CO_2 laser lines resulting in the 260 μm (1.15 THz) output. This peak power corresponds to a $\sim 2 \times 10^{-4}$

external conversion efficiency. Assuming plane-wave pumping of the GaAs crystal, one can estimate the output of DFG power for a perfect phase matching by

$$P_{THz} = 0.5 \left(\frac{\mu_0}{\varepsilon_0} \right)^{0.5} \left(\frac{4 d_{eff}^{2} \omega_3^{2}}{n_1 n_2 n_3 c^2} \right) \frac{P_{10.3} P_{10.6} L^2 T_1 T_2 T_3}{S} e^{-\alpha L}, \qquad (5.6)$$

where S denotes the area of the input beams, T_1, T_2 and T_3 are the single surface transmission coefficients at the frequencies ω_1, ω_2 and ω_3 and α is the absorption coefficient of the THz radiation in GaAs. The interaction length L in the case of noncollinear geometry is limited by the length over which two crossed beams overlap.

The best matching between the measured width of the phase-matching curve in Fig. 5.5 and a calculated one was found to be at L ~2.5 cm. Using $n_1 \approx n_2 = 3.28$, $n_3 = 3.61$ [49], the effective nonlinear coefficient for the polarization parallel to the [111] crystal axis $d_{eff} = (2/\sqrt{3})$ $d^{eo} = 50 \times 10^{-12}$ m/V, and the absorption coefficient for the THz radiation in GaAs at room temperature of 0.2 cm^{-1} in Eq. 5.6 gives $P_{260} = 2.4$ kW.

As seen in Fig 5.7, the DFG power in room temperature GaAs decreases below 1 kW level at 100 µm due to the strong absorption in the phonon band. The contribution of the absorption factor can be clearly seen by the comparison of the experimental data with the curve calculated with no absorption (see solid line in Fig. 5.7). When using the absorption as a fitting parameter in Eq. 5.6 for the GaAs sample, we obtained a value of approximately 2 cm^{-1} at 110 µm. However, cooling of the crystal to ~ 80 K decreases the absorption [42] and can be used to obtain a power above 1kW for the whole range of 1-3 THz.

5.2.3 Results in THz generation using GaSe

As mentioned in Sec. 5.2.1, a grating was used as a beam combiner to obtain two overlapped CO_2 laser beams for collinear phase matching. The polarization for the CO_2 laser beams matched the one required for Type II $\omega_3 = \omega_1 - \omega_2$ (e-oe) three frequency interaction.
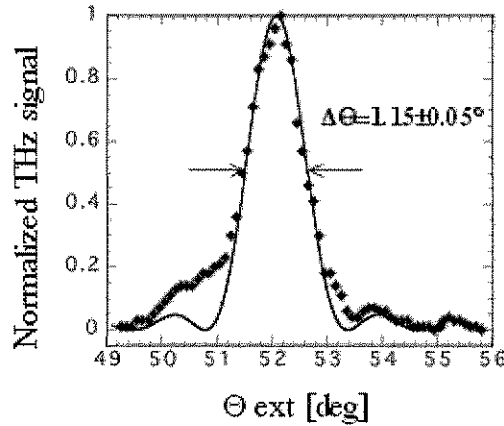
Figure 5.8 Phase matching tuning curve for 2 THz radiation generated in a 1-cm long GaSe pumped by CO_2 laser lines. The diamonds are experimental data and the solid curve represents a calculated phase mismatch function $Sinc^2(\Delta kL/2)$ fit to the experimental $\Delta\Theta$ value.

Fig. 5.8 shows the relative output power of the difference–frequency radiation versus the external phase matching angle Θ_{ext} for mixing the 9.59 μm (the 9P(24) line) and 10.22 μm (the 10R(24) line) beams. The generated frequency around 2 THz (150.26 μm) was very close to the cutoff frequency determined by the total internal reflection in GaSe. The output power peaked at $\Theta_{ext}=52°$, which is in excellent agreement with the calculated value in Fig. 5.2. The measured energy was ~10 μJ or a peak power of 50 W assuming a

200-ns long THz pulse. This power was generated with an approximately 4 MW pump power per line. To confirm the phase matching conditions, the other pair of CO_2 laser lines was mixed in the GaSe crystal and a ~1THz (289.22 μm) pulse was recorded with an output 4 times smaller than that at 2 THz.

The measured value of the width of the phase matching curve (diamonds in Fig. 5.8) was 1.15°±0.05°. This width was not consistent with that expected of a 1-cm long GaSe crystal based on the Sellmeier coefficients [52]. Note that a similar dependence was recorded for the 1.2 cm long sample. It indicated that the effective length of the crystal was independent of the actual crystal length. The best fit of phase mismatch $Sinc^2(\Delta k L_{eff}/2)$ function, where the momentum mismatch for DFG with collinear beams is $\Delta k = k_3-k_1+k_2=(n_3\omega_3-n_1\omega_1+n_2\omega_2)/c$, was obtained at L_{eff}=0.39 cm. This experimental effective length was used for further calculations. Typically, the effective length for birefringent materials is limited by the walk-off effect. But for the large pump beams ~0.6 cm in diameter utilized in the experiment this was not the case. We believe that, the main limitation on the effective length in the samples was imposed by absorption of the THz radiation.

By using a 289.2 μm beam generated in GaAs, we measured the absorption coefficient in the GaSe samples using a laser calorimetry technique. Note that this method is rather accurate and allows one to measure α at 0.02 cm^{-1} level for a 1-cm long sample [53]. At normal incidence on the crystal surface we measured transmission of the THz beam. The following expression was used to obtain the value of the absorption coefficient:

67

$$\alpha = -\frac{1}{L_c} \ln\left(\left\{ \left[\frac{(1-R)^2}{2TR^2} \right]^2 + \frac{1}{R^2} \right\}^{\frac{1}{2}} - \frac{(1-R)^2}{2TR^2} \right) \quad , \qquad (5.7)$$

where L_c is the length of the crystal, T is the transmission, and $R=(n-1)^2/(n+1)^2$ is the Fresnel power reflection coefficient of GaSe. The absorption coefficient for extraordinary polarization was found to be 3.19±3% cm^{-1} (3.25 cm^{-1} for the long sample).

Before comparing the measured and the calculated THz power, we measured the nonlinear coefficient for GaSe, since the only data on the electro-optic coefficient for this material were taken at the 0.5-1 μm range (see Table 6). By generating radiation at 289.2 μm in both a GaSe sample and a 700-μm thick GaAs wafer under the same conditions, we directly compared the effective nonlinear coefficient d_{eff} (GaSe) with a well known d_{eff}(GaAs). The length of the GaAs wafer was slightly smaller than the coherence length for this material providing conditions for the collinear phase matching. The measured d_{eff}(GaSe)/d_{eff}(GaAs) was equal to 0.46. For type II DFG the effective nonlinearity expression in the phase-matching direction is given by [52]

$$d_{eff} = d_{22}^{eo} \cos^2 \theta \cos 3\varphi, \qquad (5.8)$$

where φ is the athimutal angle and was equal to zero.

Then, by applying d_{eff}(GaAs)=50 pm/V and Θ=17.2°, the measured electro-optic nonlinear coefficient for THz generation in GaSe is 24.3±10% pm/V. It should be noted that the measured coefficient is close to that determined by using the linear electro-optic effect[10] (17±5% pm/V) but a factor of two smaller than the one measured for pure electron susceptibility in the high frequency optical range (54±10.8 pm/V) [52]. Using the

measured value of GaSe nonlinearity, the calculated power at 2 THz from Eq. 5.6 was 52 W for L_{eff}=0.39 cm and S=0.28 cm^2. Thus, the calculated and experimental powers are in a very good agreement.

To summarize, we have demonstrated a 0.5-3 THz tunable source with a kW-level of power. The THz radiation is generated in a noncollinearly phase-matched GaAs at room temperature and pumped by a compact, dual-beam TEA CO_2 laser system running at 1 Hz. The THz pulses with ~kW power are sufficient for seeding a FEL amplifier and studying FEL microbunching. However, 200ns pump pulses will need to be filtered out from the amplified pulses with ~MW level of power and duration of 15ps. In Sec. 6.2, we will discuss the filtering using a built Fabry-Perot interferometer. In the next section, we will demonstrate that DFG in a GaAs crystal can be also used to generate a pulse with a duration around ~100ps and ~MW level of power by pumping it with our Neptune TW CO_2 laser system.

5.3 High power single shot THz seed source

A narrow-band THz pulse with a $\sim$1MW level of power at present can only be generated on very few lines by using an optically pump molecular laser [54]. We generated a $\sim$1kW power pulse in noncolinear phase-matching configuration by using DFG in a GaAs crystal at room temperature with a total pump power 16MW/cm^2. By increasing the pump power, one can increase the conversion efficiency and therefore the THz power. However, for frequency mixing of 200 ns CO_2 laser pulses, the efficiency is limited by surface damage threshold of the nonlinear crystal (GaAs 30 MW/cm^2). It is known that switching to shorter pulses should increase the surface damage threshold of the material and may result in reaching higher conversion efficiency. Thus, switching to shorter $\sim$250 ps pulses with mutlti-gigawatt level of power may increase the frequency conversion efficiency in two ways: first owing to the pump power increase in the experiment and second, this power can be coupled into a crystal without damaging it. In this section, we apply the same DFG technique as discussed above and use a TW CO_2 laser system in the Neptune Laboratory as the pump source in order to generate a THz pulse with $\sim$MW peak power.

The experiment has been performed with the two-wavelength, TW CO_2 master oscillator-power amplifier system [41]. The experimental setup is very similar to one in Fig. 5.4 and the simplified optical scheme is shown in Fig. 5.9. It is important to note that in this high power study, both optical arms contain two wavelengths because of the nature of the TW CO_2 laser system.
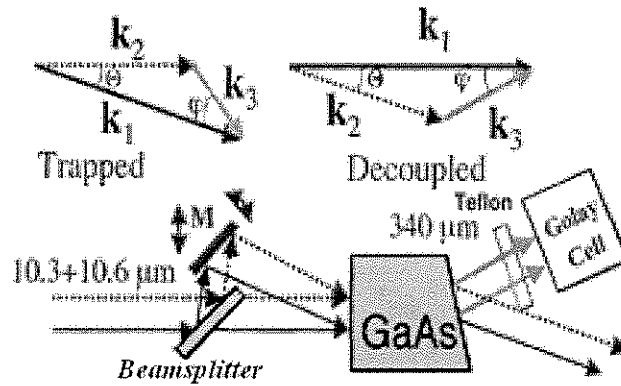
Figure 5.9 Schematic vector diagrams for noncollinear DFG inside the GaAs crystal and simplified optical scheme of the high power single shot THz seed source

Due to the complexity of the TW laser system, we only chose a particular pair of CO_2 lines for mixing: 10R(16) line at 10.3 μm (ω_1) and the 10P(20) line at 10.6 μm (ω_2). The conservation of photon energy (ω-matching) gives the wavelength of the difference-frequency radiation at 340 μm (ω_3). The phase-matching angle θ for this pair of lines is equal 0.72° (the external phase-matching angle θ_E is 2.38°) and the angle ϕ at which the THz radiation is generated with respect to the direction of incident radiation at ω_1 is 21.64°.

In the experiment a vertically polarized, two-wavelength CO_2 laser beam with duration of 250~ps was split into two optical arms and combined together in the same GaAs crystal described in Sec. 5.2. Because of the crystal geometry, only one wavelength in each arm was utilized for the DFG process of interest, and half of the THz radiation with mirror symmetric k-matching was trapped inside the crystal. Three beams (ω_1, ω_2 and ω_3) had the same polarization parallel to the [111] axis of the GaAs crystal. The THz radiation was collected by a cone and sent onto a Golay cell for detection.

For 200 ns pulses no damage was observed with intensities ≤ 16 MW/cm^2, which is in

a good agreement with a 30 MW/cm^2 value of the surface damage threshold reported by

Gordon et al [55]. In a series of damage threshold measurements for 250 ps CO_2 laser

pulses, we observed a single shot damage of GaAs at ~0.5 J/cm^2 (≤ 2 GW/cm^2). However,

in the experiment for the unfocused 10-µm beams with a cross-section of 3x2 cm,

existence of hot spots seriously limited the incident fluence especially for the multi-shot

exposure. As a result, the typical pump intensity did not exceed 1 GW/cm^2. Moreover,

using a two-wavelength beam in each arm with a 10/1 –20/1 ratio between the 10.6 and

10.3 µm lines in combination with an efficiency of the beam splitter ~0.7 caused the useful

pump power to be around 250 MW/cm^2. As shown in Fig. 5.9, a phase-matched THz beam

produced by another part of the pump with the symmetric k-matching was trapped inside

the crystal. The detector placed after a 0.5-m long Cu waveguide and teflon filters

measured approximately 250 µJ energy; taking into account the measured attenuation of

the THz transport system up to 0.5 mJ energy was generated. The results of high-power

DFG measurements are presented in Fig. 5.10. The measured width of the phase-matching

curve is very close to one in Fig. 5.5 indicating that again the interaction length is equal to

the crystal size.
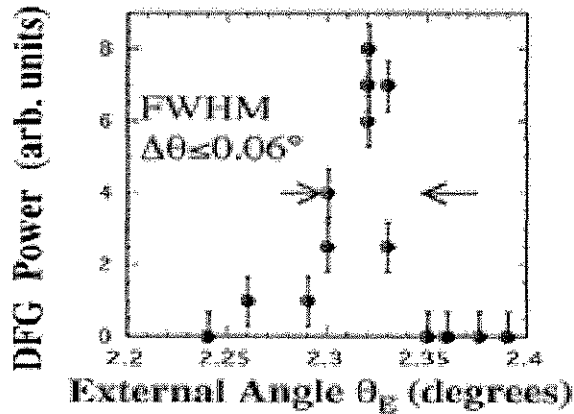
Figure 5.10 DFG output power at 340 μm versus external phase-matching angle θ_E for 250-ps long CO_2 laser pulses measured in GaAs for an unfocused beam.

If we consider the interaction length equal to the crystal size of 2.5 cm and the pump power value of 250 MW/cm^2 over the whole 6 cm^2 beam, we calculate a total power of P_{340}=2.8 MW using Eq. 5.6. This is in good agreement with the experimentally measured power of approximately 2 MW assuming a 250 ps long THz pulse. The inhomogeneity of the pump optical beam may in part be responsible for the discrepancy between the experiment and the calculations. The achieved peak power corresponds to the ~10^{-3} external conversion efficiency and represents an improvement by a factor of 500 of the peak power obtained previously by DFG in nonlinear crystals.
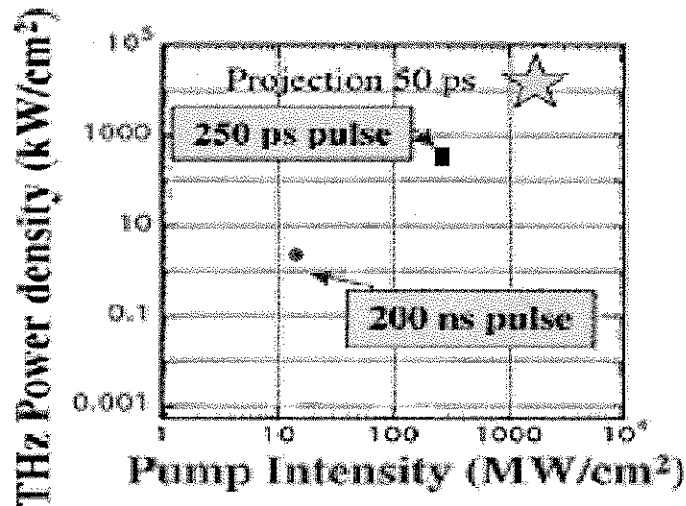
Figure 5.11 Measured THz output power density at 340 μm versus pump intensity for 200 ns long (circle) and 250-ps long (square) CO₂ laser pulses. The star mark represents the projected power value for 50 ps laser pulses

In Fig. 5.11 we combine data on THz power obtained here and Sec. 5.2. Clearly switching from 200 ns to 250 ps CO_2 laser pulses allowed for a significant increase in the conversion efficiency. This is mainly due to the increased damage threshold of GaAs for the subnanosecond pulses. A further increase in the THz power is expected from pumping the crystal by one wavelength beam in each arm and/or from switching to even shorter, 50 ps CO_2 laser pulses for which the damage threshold is expected to increase (projected power shown as a star mark in Fig. 5.11). The power level of THz radiation generated by a noncollinear phase-matching scheme may be scalable to the 100 MW level by increasing the crystal aperture. A typical beam diameter of the Neptune two-wavelength CO_2 laser system is 12 cm. This beam, in combination with commercially available large-aperture GaAs crystals (diameter 10 cm), opens the possibility of creating a very high-power source of coherent radiation tunable in the range of 0.1-3 THz.

74

Alternative approach is to use a large-aperture quasi-phase-matched GaAs structure for production of high-power THz radiation pulses. Towards this end, we have developed an original technology for Teflon bonding of GaAs wafers [56]. Despite the fact that quasi-phase-matched nonlinearity is smaller than a regular phase-matched one, a simple-for-alignment, drop-off device is potentially able to generate ~1-3MW pulses for a 4" diameter structure.

As we showed in this section, we can use the DFG technique to generate a THz pulse with MW level of power suitable for IFEL microbunching. However, the limitation of being a single-shot radiation source (every 5 minutes) and the complexity in operating with the TW CO_2 laser system makes IFEL microbunching a less preferable experimental scheme in comparison with the THz FEL amplifier/buncher.

6. Development of THz optical devices, and FEL experiment

6.1 Guiding of the THz radiation in a hollow metallic waveguide

Due to its longer wavelength, a THz pulse diffracts faster in comparison with an optical pulse. Therefore, for an IFEL/FEL microbuncher or a seeded FEL amplifier with a length on the order of 2 meters, it is important to study guiding of a THz pulse through a hollow waveguide. The function of the waveguide is to confine the THz radiation on axis so it can act back on the electron beam, and to preserve the linear polarization. For a narrowband THz pulse, the dispersion in a properly designed waveguide is negligible. The main concern for guiding is the transmission through a hollow waveguide, which is a product of the coupling efficiency and the attenuation due to resistive losses on the walls of the waveguide.

Coupling of a THz beam into a metallic hollow waveguide with a diameter of ~5mm inevitably excites multiple propagating modes, including transverse circular electric (TE), transverse circular magnetic (TM), and hybrid (EH) modes [57,58]. According to electromagnetic theory, higher order modes have larger attenuation; therefore, we consider propagation of the THz pulse in the fundamental modes of those three types. The fundamental modes are TE_{01}, TM_{01}, EH_{11} modes, respectively, and their electric field lines pattern are shown below in Fig 6.1.
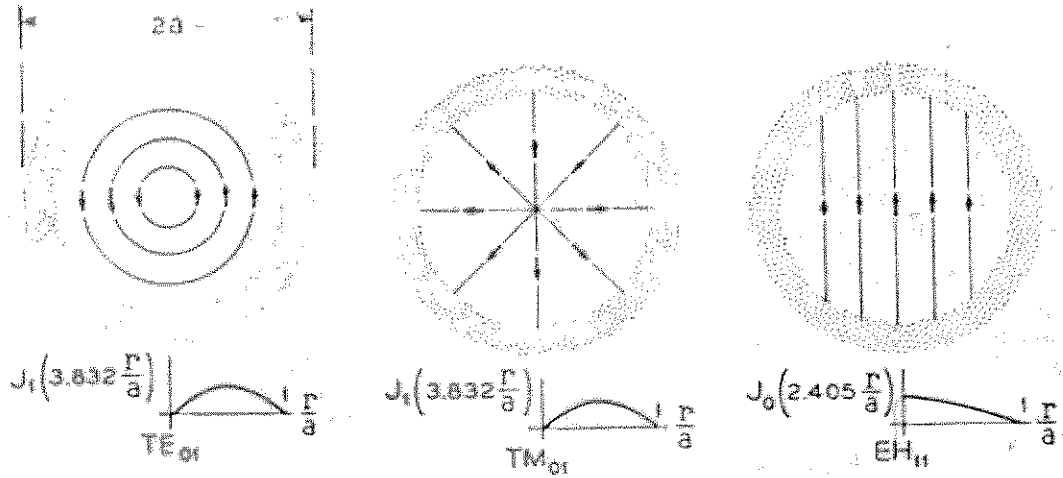
**Figure 6.1: Electric field lines of TE_{01}, TM_{01}, and EH_{11} modes
in a circular hollow waveguide**

As seen in Fig. 6.1, the field components of all propagating modes are close to zero near the boundaries, and only the transverse fields of the EH_{11} mode have maximum in the center of the waveguide. In fact, higher order hybrid modes and all TE/TM modes have no transverse field components in the middle and generally show a "donut" type structure in intensity distribution profile. Besides, the EH_{11} mode is linearly polarized therefore it is preferable for coupling a linearly polarized THz pulse in the free space into the waveguide. Thus the EH_{11} mode has an optimal intensity profile for FEL in a planar undulator. Note that in the FEL process, the THz radiation polarized in the wiggling plane of electrons is amplified and propagates along the waveguide thus the polarization would be preserved.

Theoretically, if the THz beam is focused properly at the entrance of the circular waveguide such that the ratio of the THz spot size (w_o) and the waveguide internal radius (a) is $w_o/a \sim 0.65$, up to 98% of power can be coupled from the free space Gaussian mode into the EH_{11} mode [59]. Our guiding measurements of a 10μm CO_2 laser pulse in circular

stainless steel waveguides using a calorimeter and a Pyroelectric camera confirmed the coupling efficiency and the beam profile for the EH_{11} mode [60]. Note that for the THz radiation, the EH_{11} mode size inside the 5mm circular waveguide is around 3mm in diameter, and it covers the whole wiggling motion amplitude (< 700 μm) of the electron beam plus the electron beam size ($\sigma_{r.m.s}$ < 220 μm.) for the cases we discussed in Chapter 3 and Chapter 4.

Besides considering guiding in a circular waveguide, we also tested a rectangular waveguide. Theoretically, the coupling efficiency to the rectangular TE_{01} mode in the rectangular waveguide (preferable for FEL interaction) is less than that to the EH_{11} mode in the circular waveguide because of the similarity of beam profiles to the Gaussian mode [59]. As for attenuation for those two modes in two different shapes of waveguides, electromagnetic theory predicts a higher attenuation in the rectangular waveguide due to stronger fields on the surfaces of waveguide.

To study the guiding of a THz pulse quantitatively, we carried out a series of measurements. The experiments were done using a THz pulse with a wavelength of 289 μm generated by the high repetition rate THz radiation source described in Sec. 5.2. A small part of the THz pulse was split by a GaAs wafer and sent to a Golay detector as a reference. The main pulse was focused on the entrance of a waveguide and a second Golay detector was used to measure the transmitted radiation. Both circular and rectangular waveguides made of Copper and Aluminum with various lengths were tested.

The experiments on transmission show that the coupling efficiency for the 5mm circular waveguide is slightly higher than that of the rectangular waveguide with a cross

section 4.4mm x10.6mm (WR42) and the attenuation losses on the walls are also much less. Therefore, transmission through a circular waveguide is higher than that through a rectangular waveguide as expected. Up to 90 % transmission was measured in a 50- cm long circular waveguide compared to 50% in a rectangular one with a similar length. However, a recent study done by the Dr. Harrington group (Rutgers University) showed that in a circular hollow metallic waveguide, the EH_{11} mode of a THz pulse is damped after a distance around 1 m and the propagating mode is predominately the circular TE_{01} mode [61]. We did not study the THz beam profile; therefore, a further investigation to verify the beam profile of the propagating mode is needed. If attenuation of the EH_{11} mode is indeed higher in this frequency range, one possible solution to preserve the EH_{11} mode is to coat the inner surface of the waveguide with a dielectric coating [61].

6.2 Scanning Fabry-Perot interferometer

As discussed in Sec. 4.1, a seeded FEL amplifier can provide a high power THz pulse with duration comparable to the driving electron beam. For many applications, a short (~10 ps) THz pulse with a high contrast is needed. Therefore, it is desirable to separate the amplified 10ps THz pulse from the original 200ns THz seed. Considering tunability of the FEL amplifier, we propose to use a scanning Fabry–Perot interferometer (FPI) as a filter [62-64].
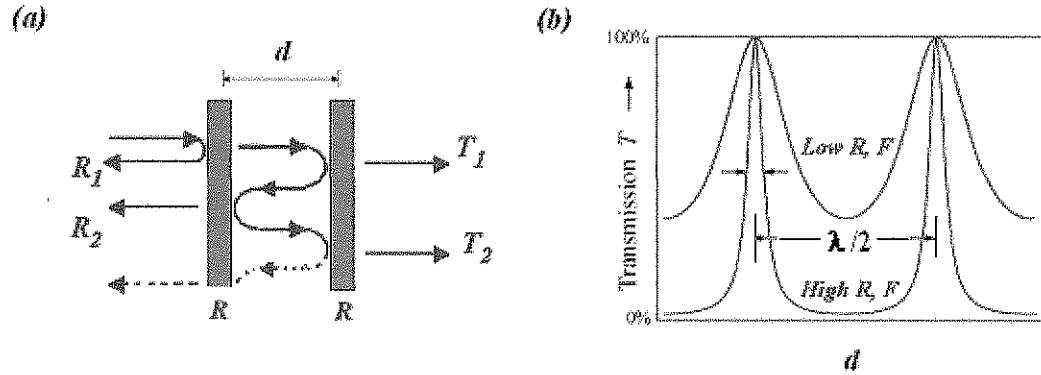
Figure 6.2: (a) Principle of operation of a Fabry-Perot interferometer and (b) its transmission as a function of the distance between two reflecting surfaces d

As seen in Fig.6.2 (a), a Fabry-Perot interferometer is typically made of two parallel highly reflecting optics. A Fabry-Perot interferometer differs from a Fabry-Perot etalon by capability to tune the distance d between the plates in order to change the wavelengths at which transmission peaks occur in the interferometer. The varying transmission function is caused by interference between the multiple reflections of light between the two reflecting surfaces (R_1, R_2...). If the both plates have a reflection coefficient R, the

transmission function is given by:

$$T(\lambda,d) = \frac{(1-R)^2}{1+R^2 - 2R\cos(\frac{4\pi}{\lambda}d)} = \frac{1}{1+F\sin^2(\frac{2\pi}{\lambda}d)} \qquad (6.1)$$

, where $F = \dfrac{4R}{(1-R)^2}$ is the coefficient of finesse.

Maximum transmission T=1 occurs when the optical path length difference ($2d$) between each transmitted beam is an integer multiple of the wavelength (constructive interference). However, when the path-length difference is equal to half an odd multiple of the wavelength, the transmitted beams are out-of-phase, destructive interference occurs and this corresponds to a transmission minimum (shown in Fig. 6.2 (b)). Note that the higher the reflection coefficient R (thus higher the finesse), the narrower the FPI peaks peaks.

In far-infrared optics, optical properties of metallic mesh structure have been studied theoretically and experimentally as a filter, a beam splitter, and a reflector [65,66]. Currently, a freestanding wire grid polarizer made of tungsten is commercially available with a reflectivity R > 99.9% at 1 THz [67]. Therefore, we used a pair of such polarizers with a diameter equal to 2" to build a scanning FPI with a high finesse. The picture of the built FPI is shown in Fig.6.3. As seen in Fig. 6.3, one wire grid reflector is fixed and the other is mounted on a translation stage with a computer-controlled actuator. Therefore, the distance between these two reflectors can be scanned and the system can be easily integrated with other automated diagnostics.
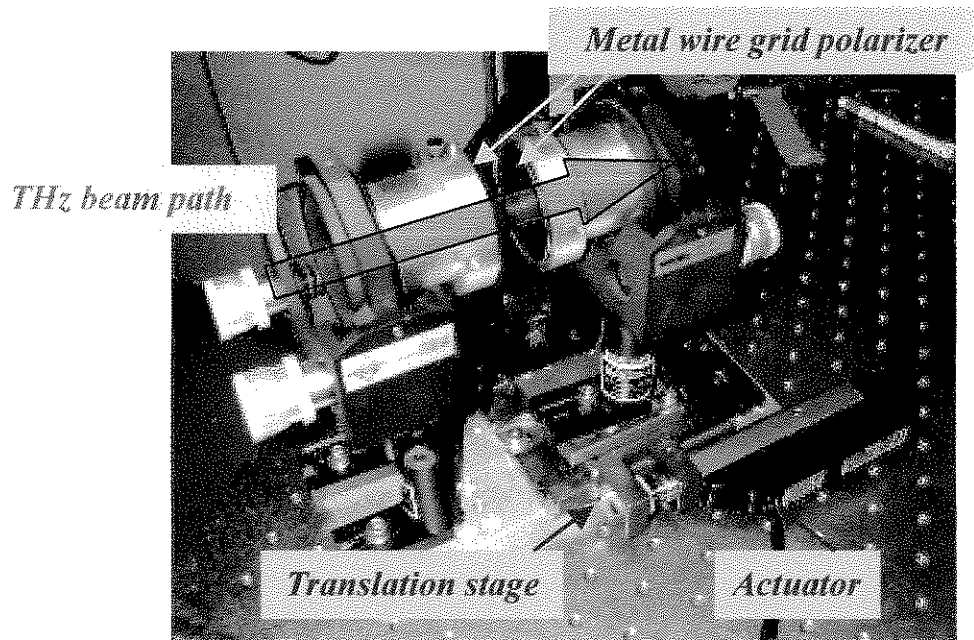
Figure 6.3: Scanning Fabry-Perot Interferometer

As reported in Sec. 5.2.2 (Fig.5.6), this scanning FPI has been used to measure the spectral bandwidth of a 200ns long THz pulse. As shown in Fig. 5.6, several transmission peaks are observed while scanning the distance between d and the separation between peaks is in good agreement with the theoretical value of $\lambda/2$. Note that when the separation between two metal wire grids is ~ 10 mm, the bandwidth of the FPI is around ~ 400 MHz scale which is larger than both the intrinsic bandwidth of the THz pulse (determined by the bandwidth of the pump CO_2 lasers of pump and nonlinear frequency mixing) and the transform-limited bandwidth of a 200 ns pulse (~ 5 MHz). Therefore, the peak transmission for a long pulse should be close to 100%, if the resonant distance carefully tuned. Note that the overall finesse is not only dependent on the reflectivity of the wire

grid but also the surface defects, such as flatness of the plate, and the optical geometry. The over-all finesse of our system is around 1000.

We can look at the property of the FPI from another prospective. Physically, a THz pulse with duration shorter than the filling time of this Fabry-Perot cavity (on the ~10 ns scale) is unable to create multiple bounces and would be reflected back. Therefore, we can use FPI as a filter for two different pulses having very different pulse durations.

This FPI can be applied to filter out the amplified THz pulse discussed in Sec. 4.1. The principle of FPI filter is illustrated in Fig. 6.4. As seen in Fig. 6.4, for the longer seed pulse (200ns), the F-P cavity is filled up and multiple reflections create a constructive interference in transmission. For the short 10ps pulse, the distant between two plates is too long to build up interference based on multiple reflections and the short pulse would be directly reflected by the first surface. Therefore, according to our estimation, the contrast of the 10 ps THz pulse to long 200 ns pulse can be improved up to 10^4 in a single pass.
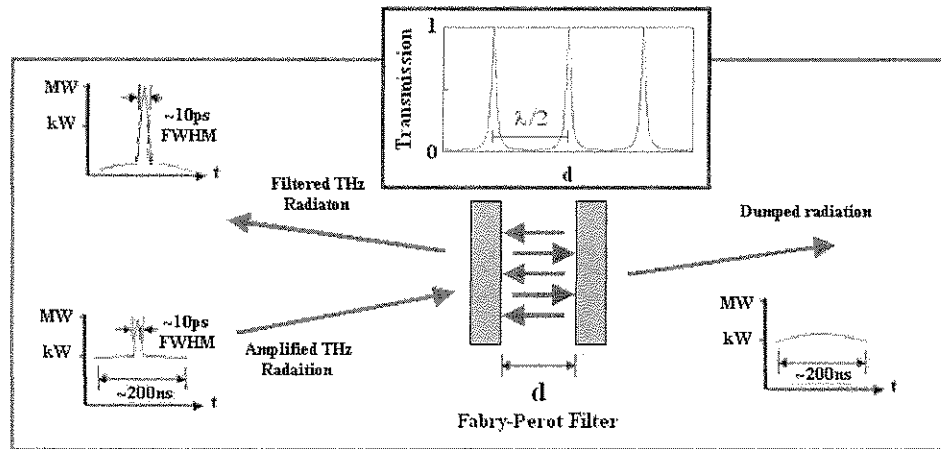
Figure   6.4:   Improving the THz contrast by using a Farbry-Perot filter

6.3 Measurements of FEL Spontaneous Emission using a grating spectrometer

As discussed in the previous section, the Fabry Perot Interferometer can be used to study the frequency content of a radiation pulse in the THz range. However, the narrow bandwidth of FPI limits its applicability only for radiation with a relatively long pulse duration. We have built another diagnostic system based on a diffraction grating, which is easy to use and widely utilized for spectral measurements at the optical wavelength [68-70]. Our goal is to develop a grating spectrometer capable to resolve the THz undulator radiation both in SASE and FEL amplifier regimes. This is a critical point in tuning energy of the electron beam to the resonant wavelength of the FEL.
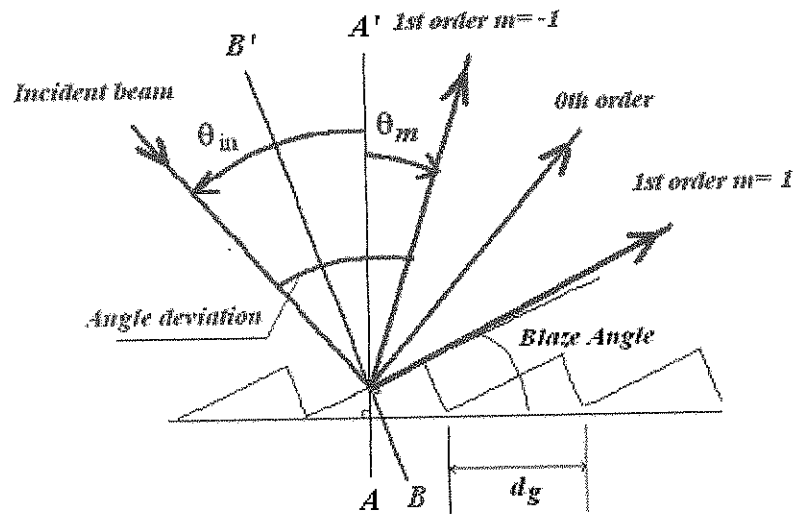
Figure 6.5: Diffraction grating

A diffraction grating is an optical component with a surface covered by a regular pattern of parallel lines, typically separated by a distance comparable to the wavelength of

84

longer (3.3 cm) to take advantage of the existing mechanical design, and the K factor is set

to be lower to ease the requirements for making magnets very close to the Halbach limit.

After several rounds of optimization, we chose the K=2.506 and the simulation result of

the seeded FEL amplifier with the modified parameters is show in Fig. 6.14. As seen in

Fig. 6.14, the gain and saturation level for the FEL with the modified parameters is almost

identical to the previous simulation results.
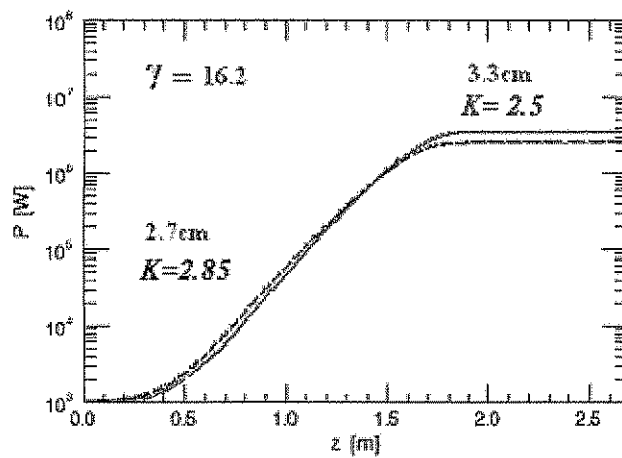
**Figure 6.14. Comparison between THz output results of (a) the original
2.7cm-period undulator (dash), (b) a modified 3.3cm-period undulator (solid)**

Currently, all these magnetic devices are being manufactured, and are expected to be

tested and ready for installation in the Neptune Laboratory in 2009.

95

7. Conclusions

To extract a mono-energetic electron beam from a high-gradient plasma based accelerating structure, externally injected beam must be prebunched in a series of ultrashort (~15-50 μm) beamlets separated exactly by period of the plasma wave in the range 100-300 μm (1-3 THz). This thesis explores possibility of using interactions between the relativistic electron beam and THz radiation for longitudinal modulation of the beam, i.e. microbunching, on the THz wavelength scale.

We carried out feasibility studies on waveguide IFEL and FEL microbunching using numerical codes *TREDI* and *GENESIS 1.3*, respectively. The simulation results showed that both microbunching techniques can be realized and tested in the Neptune Laboratory-- a university scale research laboratory-- because of (i) modest requirements on parameters of the electron beam from a photoinjector, (ii) a relatively compact and easy to build undulator, and (iii) achievable radiation power of a narrowband THz seed. According to the simulation results, up to 50% of particles can be bunched within $\lambda/7$ (FWHM) and each bunch is separated by the same periodicity as the seed THz pulse. IFEL microbunching has the advantage in forming uniform microbunches for the whole length of the beam, and only needs a ~30-cm-long undulator pumped with a ~MW THz pulse. As for seeded FEL microbunching, a tunable seed source in the range of 0.5-3 THz with a power around 1kW is sufficient to demonstrate microbunching in a ~2 m-long undulator driven by an electron beam with a peak current of 40 A (400 pC of charge). However, slippage effect in this case causes inhomogeneous microbunching.

It is important that during resonant interaction between the relativistic electron beam and the THz radiation pulse in the presence of magnetic field (FEL interaction), the radiation pulse is amplified. According to the simulation results, the 2 m-long FEL undulator when driven by an electron beam with a peak current of 60A can be used as a single pass THz amplifier with a gain of $\sim$2x10^4 (power increases from 1kW to $\sim$20MW) tunable in the 0.5-3 THz range. The frequency range can be further expanded to up to 9 THz via the HGHG FEL configuration, where $\sim$100 % power conversion efficiency from the 1-3 THz seed radiation to the third harmonic can be achieved with a MW level of seed power in a 30 cm long prebuncher followed by the 2-m long radiator. It is even possible to reach a peak power of 100MW, if an electron beam with a peak current of 100A is used. Such high-power, narrowband THz pulses, will be 50 times more powerful than currently available worldwide, and can open new opportunities for studies on nonlinear optics, material properties of semiconductors [72] and bio-molecular objects.

None of the above mentioned applications are possible without narrowband THz radiation seed sources. We reported the development of THz radiation sources by mixing of two CO_2 laser lines in a non-collinearly phase matched GaAs at room temperature. For the IFEL microbunching, we generated a $\sim$200ps-long THz pulse with up to 2MW of peak power, which is the highest power ever achieved using DFG in a nonlinear crystal. This was achieved by using a multigigawatt pulses from a TW class CO_2 laser system in the Neptune Lab [27]. We also built and characterized a tunable THz seed source pumped by a high repetition rate, dual-beam TEA CO_2 laser [26]. The 200ns THz pulse with a peak power of $\sim$1kW is suitable for seeding a FEL microbuncher/amplifier. Availability of a

tunable THz source running at 1 Hz made it possible to study THz wave guiding which is a critical issue for the 2-m long FEL. It is important to note that by using commercial CO_2 lasers running at 30-100 Hz range, mW level of average power can be reached.

Entering the THz range of wavelengths required building of several original tools and diagnostics. We have built a Fabry-Perot interferometer that also doubles as a filter for a short (~10ps) narrowband THz pulse. The filter is of great use for obtaining a high contrast THz pulse from the seeded FEL amplifier driven by a short electron beam. We also developed a diffraction grating spectrometer, which can be operated in the wavelength range of 70-340 μm. The spectrometer is important for tuning the electron beam energy to the resonant wavelength of the FEL and for the spectral analysis of FEL radiation.

In summary, the numerical feasibility analysis, the THz source development, the short pulse filter, and to the diagnostic for the spectral measurement, presented in this thesis give us reasons to believe that the upcoming seeded FEL microbuncher/amplifier and HGHG FEL experiments in the Neptune Laboratory will be successful. These investigations are crucial for demonstration of the Plasma LINAC concept for advanced plasma accelerators and for a future high-power, narrow-band THz radiation user facility for high-field science.

APPENDIX A

Laser bearwave microbunching in vacuum

Laser Beat-Wave (LBW) microbunching in vacuum is an alternative way to modulate a relativistic electron beam on the THz scale [73]. As was shown theoretically, a high-power LBW modulates the axial momentum of a co-propagating relativistic electron beam [74,75,76]. The interaction between the electron beam and the LBW in vacuum modulates the electron momentum at the frequency of the beat envelope associated with interference of the two laser lines and can be easily tuned to the THz spectral range. It can also be seen as a "magnet-free" IFEL microbunching, since one of the laser pulses works as the undulator to wiggle the electron beam transversely.

In this appendix, we review physics of the LBW interactions with the electron beam and simulate the LBW Microbunching experiment at the UCLA Neptune Laboratory using 3D FEL code Genesis 1.3. Then, we describe the experimental set-up, followed by detail discussion of results.

A-1. Physics of Laser Beat-Wave Microbunching

To study the ponderomotive acceleration and energy modulation of a relativistic electron beam by a LBW, we used the model described by D. Gordon et al. [74].

The electric field of the linear polarized fundamental Gaussian beam with the transverse component Ex and the longitudinal component Ez is given by

99

$$E_x = E_0 \frac{w_0}{w} \exp\left(-\frac{r^2}{w^2}\right) \cos\phi$$

and

$$E_z = 2E_0 \frac{w_0}{w} \frac{x}{kw^2} \exp\left(-\frac{r^2}{w^2}\right)\left(\sin\phi - \frac{z}{Z_r}\cos\phi\right)$$

where x is the transverse position with respect to the laser axis, z is the longitudinal position with respect to the waist position, Z_r is the Rayleigh length, k is the wavenumber, w_0 the spot size at the best focus and $w(z)=w_0\sqrt{1+(z/Z_r)^2}$ is the spot size at a given z, E_0 is the field amplitude and the phase at the laser frequency is given by

$$\phi_{0,1} = k_{0,1}z - \omega_{0,1}t + \frac{r^2}{w^2}\frac{z}{Z_r} - \tan^{-1}\left(\frac{z}{Z_r}\right).$$

The difference between the two frequencies is apparent only in the radiation phase and it is indicated by the indices 0 and 1, respectively.

The beatwave has two characteristic phases, corresponding to the sum and difference of the phases of the individual modes:

$$\phi = \frac{1}{2}(\phi_1 + \phi_2) = \tilde{k}z - \tilde{\omega}t + \frac{r^2}{w^2}\frac{z}{Z_r} - \tan^{-1}\left(\frac{z}{Z_r}\right) \quad \text{and} \quad \Phi = Kz - \Omega t$$

with $\tilde{k}$ and $\tilde{\omega}$ as the mean values of the wavenumbers and frequencies and $K=(k_0-k_1)/2$ as well as $\Omega=(\omega_0-\omega_1)/2$.

We considered a case when two fundamental Gaussian beams with different frequencies but the same waist position, size and Rayleigh length are overlaid, forming a beat wave. It can easily be shown that the strong transverse electric field excites a transverse oscillation. As a result the electrons on axis will be pushed to an off-axis

100

position and, therefore, start experiencing a non-vanishing longitudinal accelerating field E_z. The transverse position of the electron can be very well approximated from

$$x=(2\gamma/k)a(z)\cos\phi$$

, where $a(z)$ is the slowly varying part of the normalized vector potential of the laser filed given by

$$a(z) = \frac{eE_0}{kmc^2} \frac{w_0}{w(z)} \exp\left(-\frac{r^2}{w^2(z)}\right)\cos\Phi$$

If the two frequencies lie close together many wavelengths of the sum-mode as well as the optical laser field slip over an electron while it propagates through the waist of the Gaussian beam. The net impact on the electron is averaged out to zero after it leaves the $2z_0$ region. On the other hand, the slippage of the difference mode or the LBW can be comparable to the Rayleigh length owing to its slower phase velocity. This makes possible acceleration of some electrons and deceleration of others on the scale of the LBW and results in an energy modulation controlled by the nonlinear ponderomotive force.

The change in the electron energy is incorporated in the code using the analytical expression for energy modulation as

$$\frac{d\gamma}{dz} = \frac{z}{Z_r^2} \frac{\gamma a(z)^2}{1+(z/Z_r)^2}\cos^2\Phi \qquad (A.1)$$

As seen in Eq. A.1, the energy modulation of electrons is depended on the interaction phase of the LBW. Therefore, the period of the longitudinal microbunching is the same as the LBW wavelength. Note that the interaction phase Φ is integrated piece-wise with an integration step length much shorter than the Rayleigh length. All fast oscillating terms,

which are proportional to $\sin\phi$ and $\cos\phi$, are omitted in the calculation.

A-2. Experimental Scheme of THz LBWM at the Neptune Laboratory and Simulations Results
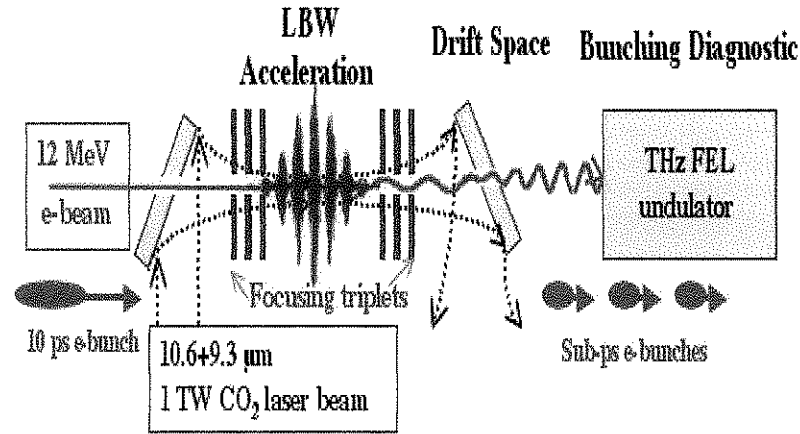

Figure A.1: Schematic of THz LBW microbunching experiment at Neptune Laboratory

The Neptune Laboratory hosts a TW class CO_2 laser, providing a natural comb of lines with the LBW in the range of 1-5 THz, and a 12 MeV photoinjector synchronized with the CO_2 laser [77]. A scheme of the LBW microbunching experiment is shown in Fig. A.1. Here the two-wavelength CO_2 laser beam with a peak power of around 1TW (200 J, 200 ps) is focused into the vacuum chamber such that the laser beam size w_0 at a $1/e^2$ level is ~180 μm providing an intensity of 1×10^{15} W/cm^2. For the experiment we consider the LBW between the 10.6 and 9.6 μm lines ($\lambda_{LBW} \approx 100$ μm) and the 10.6 and 9.3 μm lines ($\lambda_{LBW} \approx 77$ μm). A 10-ps full width at half maximum electron bunch produced by an RF

photoinjector is injected in the LBW. A 12 MeV electron beam with an energy spread of 0.5% is focused down to 200 μm (σ_{rms}) at the laser focal plane. We anticipate that bunches with a charge well in excess of 0.5 nC will be produced, providing a peak current of 60 A.

The interaction of the electron beam and the LBW results in ponderomotive acceleration and energy modulation of particles on the THz scale. This stage is followed by a ballistic drift of the electrons over approximately a 1.5 m long distance, where the gained energy modulation transfers to the beam current modulation and, therefore, THz bunching. The CO_2 laser beam is transported out of the vacuum after the laser fluence falls down to the safe level and could be recycled. However, with above-mentioned parameters, the energy modulation and current modulation due to the LBW interaction is extremely challenging to measure using conventional methods. A 33-cm long undulator magnet with a period of 3.3 cm and a K value of 1.8 is designed to be resonant to the LBW wavelength, and a quadrupole triplet is used to match the beam envelope to the natural focusing of the short undulator. A coherent start-up of THz generation takes place in the undulator owing to the current modulation. Therefore, the undulator works as a single-shot diagnostic of a bunched electron beam, since the power of THz undulator radiation is directly related to the amplitude of current modulation of the injected electrons.

Modeling was carried out for the arrangement presented in Fig. A.1 with the actual drift distances and the position of focusing magnets in the Neptune Laboratory. The rather pessimistic values of 10 keV for the intrinsic energy spread and 16 mmxmrad for the emittance were taken for the electron beam. The dynamics of the growth in the current modulation and radiation power is presented in Fig.A.2. This case has a perfect overlap of

103

the electron beam waist position with the laser beam containing 500 GW per CO_2 laser line and the LBW at 77 μm.
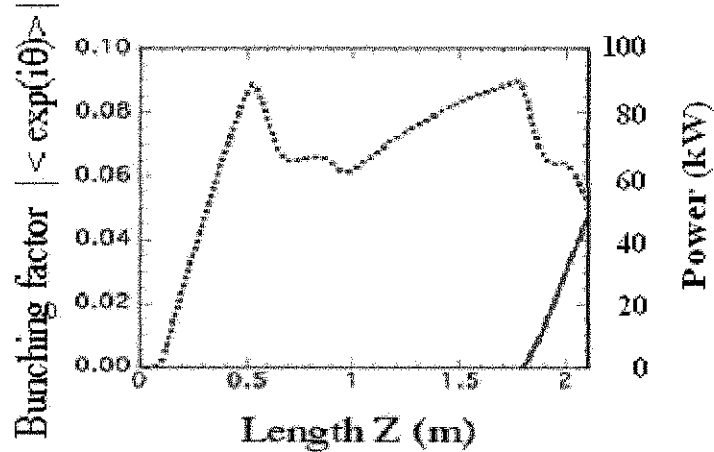

Figure A.2: The current modulation (dotted line) and the THz power at 77 μm (solid line) along the Neptune beam line.

After the LBW interaction at z=9 cm the current modulation grows almost linearly before the beam enters the focusing quadrupole triplet, the first magnet of which is located at z=36 cm. This focusing triplet is necessary to preserve the beam size until the diverging laser beam is possible to decouple from the particle beam at z=140 cm. The dispersion within the triplet slightly decreases the current modulation, however, after the quads the modulation continues to grow bringing the bunching factor to 9% at the undulator entrance plane (z=170 cm). The bunching factor F= | <exp(iθ)> |, where θ is the phase at which each electron is located inside the period of a THz wave, is proportional to the ratio of the bunch length and the separation between bunches. As seen in Fig. A.2, inside the undulator the F value decreases due to the fact that the electron beam modulation after the long drift is not linear any more or the electron beam is over-bunched. At the same time

the THz FEL radiation reaches almost 50 kW of power at 77 μm, that is two orders of magnitude above the detection threshold of the Golay cell

Due to the availability of the 33-cm long undulator with fixed parameters, we looked at the resonant energy of the electron beam to yield the maximum power at 77 μm. As seen in Fig.3a, the resonance is observed at γ=24.5, where the radiation power is reaching 60 kW.
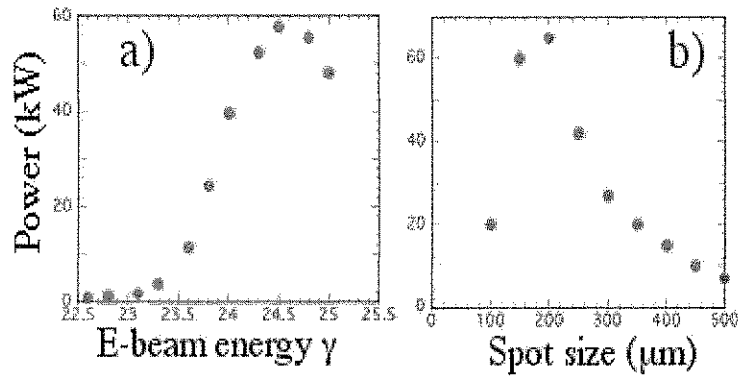

Figure A.3: Simulation results of the THz power at 77 μm as a function of (a)energy of the electron beam and (b) the laser spot size.

Fig. A.3b shows the results of the THz power optimization for different laser focal spot sizes when the electron beam size is 200 μm (σ_{rms}) and the total laser power is fixed. The maximum is achieved when the laser beam is smaller than the electron beam size. In this case the on-axis electrons see a higher laser field and being modulated more strongly emit coherently in the undulator. However, for a more uniform energy modulation of all electrons, it may be desirable to have the laser beam waist that is larger than the electron beam size. This would be a favorable mode of operation for the LBW microbunching and needs to be studied.
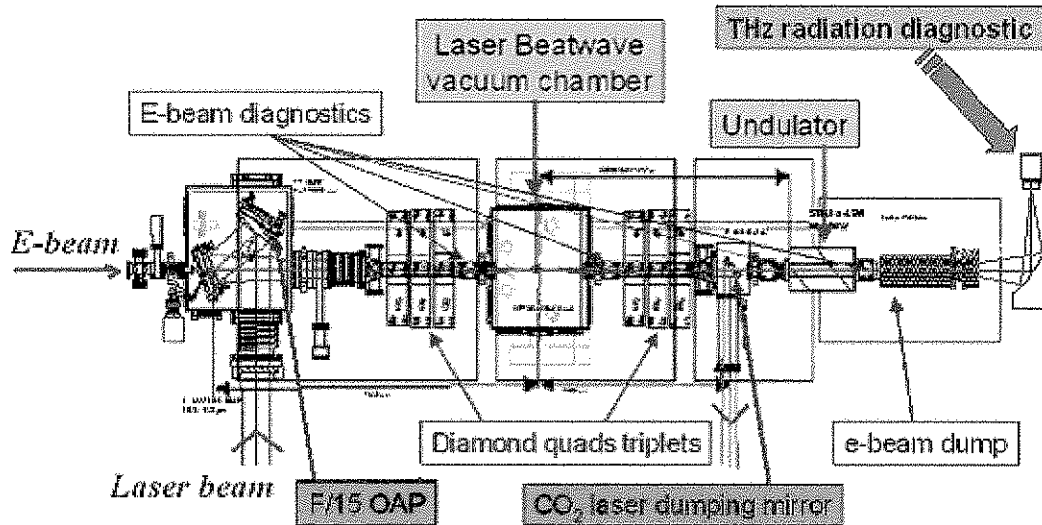
105

A-3. Setup of the THz LBWM Experiment

Figure A.4: Experimental Setup of THz LBW microbunching experiment at Neptune Laboratory

To implement the proof-of-principle experiment on Laser Beat-Wave Microbunching, we have modified both our CO_2 laser system and electron beam system in the Neptune Laboratory (Fig. A.4).

On the laser side, we changed the pair of lines from the original 10.6/10.3 μm pair to the 10.6/9.3 μm one, and focused the laser beatwave into the LBW vacuum chamber using an F/15 off-axis parabolic mirror (OAP). A longitudinal scan of the beam profile of an un-amplified CO_2 laser pulse taking by a pyro-electric camera was performed and the typical image at the focus is shown in Fig A.5. The spot size at the focus was around ~180-220 μm and Rayleigh range, Z_r, is ~12 mm.The total power of the amplified pulse

was close to 500 GW with a line ratio 3:1, i.e., the intensity of the beatwave reached to 3×10^{14} W/cm^2. The latter was verified additionally by measuring the ionization appearance intensity in Ar.
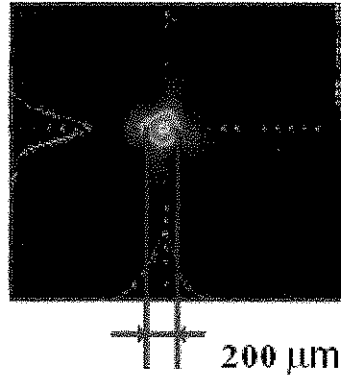

Figure A.5: The typical CO$_2$ beam profile taking by a pyro-electric camera at the focus of the LBW microbunching experiment at Neptune Laboratory

On the electron beam side, we extended the electron beam line by ~3 meters (from the end of the target chamber) to accommodate the drifting space, and the undulator. A quadrapole triplet and several steering magnets were installed to focus the electron beam into the waveguide in the middle of the 33 cm-long, planar undulator. A 6" copper mirror with a 1-cm hole was used to separate the LBW from the electron beam after the interaction. After the undulator, the THz undulator radiation is separated from the electron beam by using an electron spectrometer as an electron dump. At the end of the beam line, a silicon window was mounted at close to the Brewster angle to release the THz undulator radiation. Pictures of major experimental devices are shown in Fig. A.6. It is interesting to note that we had to bore a 1.5m-wide hole on a 3-feet-thick concrete wall in order to make room for the experiment.
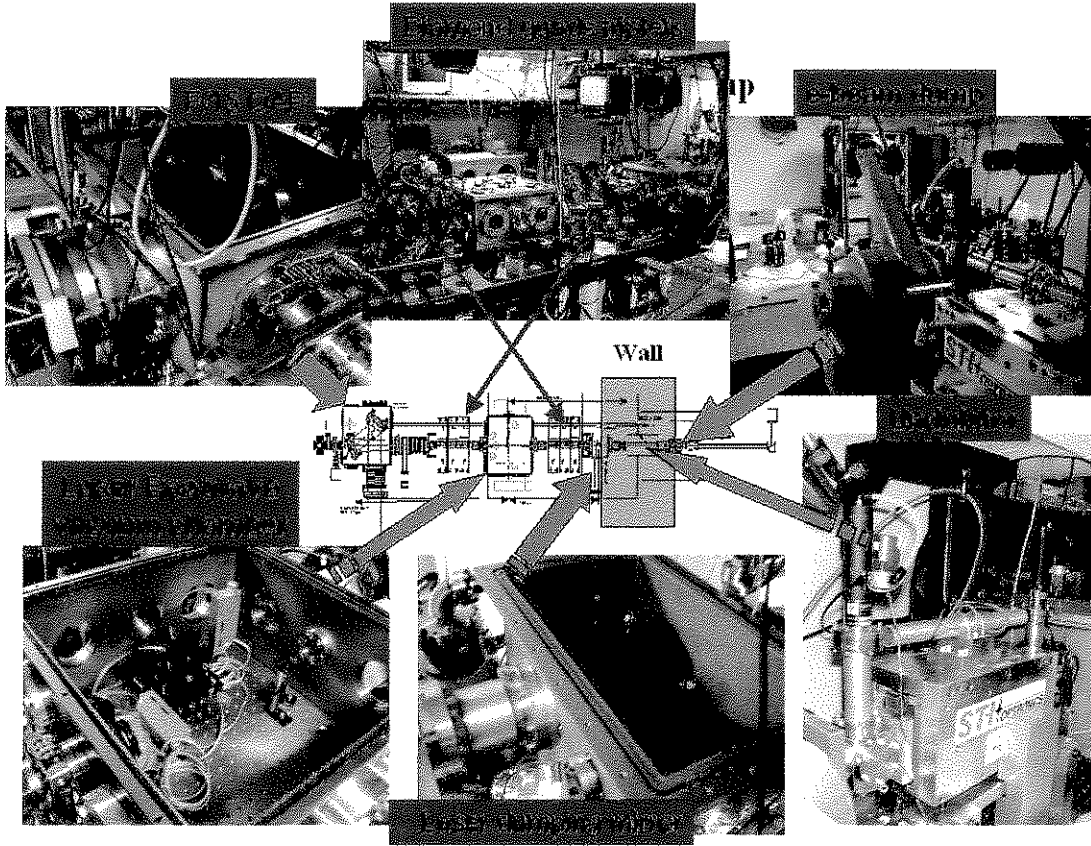
107

Figure A.6: Images of THz LBWM experimental setup at Neptune Laboratory.

To study the LBWM interaction, the LBW and the electron beam have to be both overlapped spatially and synchronized temporally at the interaction point (IP).

For the spatial overlapping, the experimental procedure consisted of two steps. First, the un-amplified laser beam was aligned through reference irises that represented the beamline axis, secondly the e-beam was sent through the same axis. In order to have precise alignment at the IP, a multi-purpose probe mounted on a computer-controlled, xyz motion actuator was inserted and observed through the side window. A camera with a resolution of 40 μm per pixel could see both the electron beam profile on the phosphorous screen and the spark produced by the focused um-amplified laser pulse on the same screen

108

with graphite substrate. This method of alignment provided $\pm 50\mu m$ residual misalignment between the beams, which was adequate for the experiment.

For the temporal synchronization, the procedure includes the nanosecond synchronization and the cross-correlation of the laser pulse and the electron bunch [78]. The nanosecond synchronization was done by a fast HgCdTe detector for the 10.6 μm pulse, and a photodiode measuring the photocathode drive laser pulse. After timing the two reference signals to within ~1 ns, cross-correlation is needed for synchronizing the electron bunch and the CO_2 laser pulse at the IP within 100 ps. Electron beam controlled transmission of the 10.6 μm radiation through the Ge crystal on the probe was utilized for the cross-correlation at the picosecond time scale [79]. For this purpose the pulse was sent through a 2-mm thick germanium plate at the laser focus and the time dependence of the 10.6 μm radiation was recorded. The latter was realized by a computer controlled optical delay line. A typical result of cross-correlation measurement is presented in Fig. A.7.

If the electrons reach the Ge plate before the CO_2 laser pulse, the 10.6 μm radiation is fully screened by the electron-hole plasma generated by the electron beam. This is seen to be the case from 0 to 150 ps in Fig. A.7. From 150 ps to approximately 400 ps, the electron bunch and the 10.6 μm pulse cross each other, resulting in increase of transmission or cross-correlation. The plasma formation in a semiconductor happens on a time scale similar to the duration of the plasma-creating electron bunch. Therefore, accuracy of the cross correlation measurements is limited by the 10 ps bunch length when the spot size of the electron beam is larger than that of the laser beam. As seen in Fig. A.7, a total width of the cross-correlation curve is ~ 250 ps, which agrees very well with the CO_2 laser pulse

length measured by a streak camera.
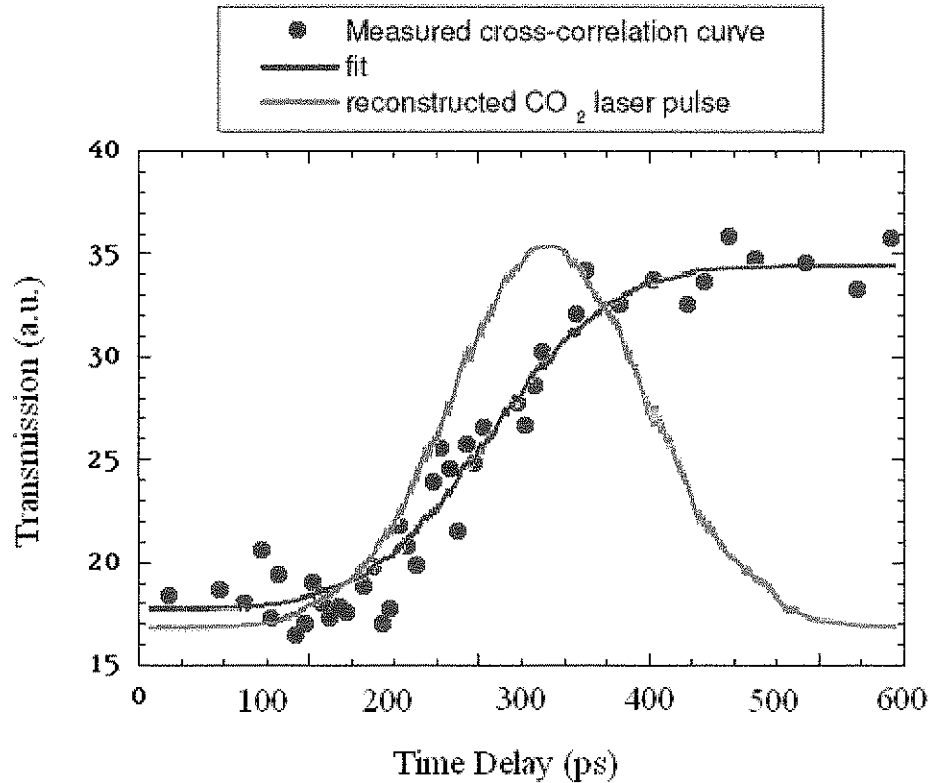
Fig. A.7: Typical electron beam/ CO_2 laser cross correlation curve

A-4. Experimental Results of LBW Microbunching and Discussions

The undulator radiation is considered to be the main diagnostic for ponderomotive LBW microbunching. The undulator radiation was collected by a 5" OAP and measured by a Golay detector behind a thick Teflon plate working as a CO_2 radiation filter. Typical measurements were obtained with an electron beam charge of 400pC and with LBW power of 500GW. While scanning the resonant electron beam energy from 11.5-12.8 MeV, we constantly observed the THz signal on the Golay detector with an amplitude of

110

150-200 mV when an additional preamplifier (gain ~ 80 times) was used. The linear scaling of the signal versus charge of the electron beam indicates that such radiation is mainly the spontaneous emission caused by spikes in longitudinal distribution of the electron beam (as discussed in Sec. 6.3). Most importantly, no correlation between the THz undulator radiation signal and power of the laser beatwave was found.
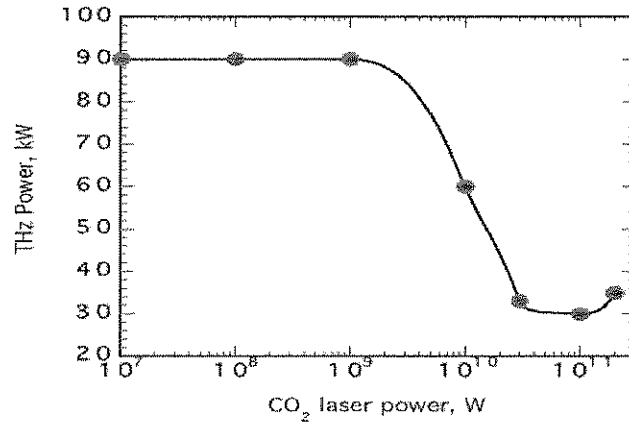

Fig. A.8: The calculated THz signal produced by LBW bunched beam as a function of 10-μm leakage

Simulations done afterward showed that the leakage of the laser beatwave through the hole of the dumping mirror can interact with the electron beam via high harmonic IFEL interaction in the undulator [80] and could result in debunching of the electron beam. This 7th harmonic coupling at 10.6 μm x 7 = 74.2 μm disrupts modulation at $\lambda_{LBW} \approx 77$ μm and, as shown in Fig. A.2, decreases the THz LBW signal by a factor of 2.5 for laser intensities around 30 GW/cm^2 reached in the experiment. This effect could be eliminated by a better separation method for the CO_2 laser pulse and the electron bunch, for instant, a magnetic dipole.

The experimental results also show that the Noise Equivalent Power (NEP) due to the

spontaneous emission of the spiky electron bunch is on the 10s of nJ scale, making measurements of LBW induced radiation at 77 μm extremely challenging. To further study the LBW microbunching, one can also try to improve the signal to noise ratio by enhancing the laser beatwave power, increasing the electron beam charge, or applying the diffraction grating spectrometer, However, we believe that improvements on the rather poor reproducibility of both the CO_2 laser system and the electron beam system in a single shot experiment is the most critical factor for measurement of LBW microbunching.

References

[1] T. Tajima and J. M. Dawson, "Laser Electron Accelerator," Phys. Rev. Lett., vol. **43**, pp. 267-270 (1979)

[2] C. E. Clayton, K. A. Marsh, A. Dyson, M. Everett, A. Lal, W. P. Leemans, R. Williams, and C. Joshi, "Ultrahigh-Gradient Acceleration of Injected Electrons by Laser-Excited Relativistic Plasma Waves," Phys. Rev. Lett., vol. **70**, pp. 37-40 (1993)

[3] A. Modena, Z. Najmudin, A. E. Dangor, C. E. Clayton, K. A. Marsh, C. Joshi, V. Malka, C. B. Darrow, C. Danson, D. Neely and F. N. Walsh, "Electron acceleration from the breaking of relativistic plasma waves," Nature, vol. **377**, pp.606-608 (1995)

[4] V. Malka, S. Fritzler, E. Lefebvre, M.-M. Aleonard, F. Burgy, J.-P. Chambaret, J.-F. Chemin, K. Krushelnick, G. Malka, S. P. D. Mangles, Z. Najmudin, M. Pittman, J.-P. Rousseau, J.-N. Scheurer, B. Walton, and A. E. Dangor, "Electron acceleration by a wake field by an intensity ultrashort laser pulse," Science, vol. **298**, pp. 1596-1600 (2002)

[5] M.J. Hogan, C. D. Barnes, C. E. Clayton, C. O'Connell, F. J. Decker, S. Deng, P. Emma, C. Huang, R. Iverson, D. K. Johnson, C. Joshi, T. Katsouleas, P. Krejcik, W. Lu, K. A. Marsh, W. B. Mori, P. Muggli, R.H. Siemann, and D. Walz, " Acceleration and focusing of electrons and positrons using a 30 GeV drive beam," Advanced Accelerator Concepts, Tenth workshop, pp. 3-10 (2002)

[6] E. Esarey, P. Sprangle, J. Krall, and A. Ting, IEEE Trans. on Plasma Science, vol. **24**, pp. 252-288 (1996)

[7] C. Sung, S. Ya. Tochitsky, P. Musumeci, et al, " Study of a THz IFEL prebuncher for laser-plasma accelerators," Advanced Acceleration Concepts, 2004, edited by V. Yakimenko, AIP conf. Proc. pp. 922-928 (2004)

[8] J.B. Murphy and C. Pellegrini, "Introduction to the Physics of the FEL", Proc. Of the South Padre Island Conf., Springer pp.163 (1986)

[9] W. D. Kimura, M. Babzien, I. Ben-Zvi, et al, "Demonstration of high-trapping efficiency and narrowenergy spread in a laser-driven accelerator," Phys. Rev. Lett., vol. **92**, 054801-1-054801-4 (2004)

[10] L. Giannessi, P. Musumeci, and M. Quattromini. "Tredi:fully 3d beam dynamics simulation of rf guns, bendings and fels," Nuclear Instruments and Methods A, 436:443 (1999)

[11] S. Reiche, Nuclear Instruments & Methods in Physics Research, Section A (Accelerators, Spectrometers, Detectors and Associated Equipment), vol.**429**, no.1-3, 11June 1999, pp. 243-8

[12] H. H. Weits and D. Oepts, " Continuously tunable, high-power, single-mode radiation from a short-pulse free-electron laser," Phys. Rev. E, Vol. **60**, pp.946 (1999)

[13] C. Sung, S. Ya. Tochitsky, S. Reiche, et al, " High gain seeded FEL Amplifier Tunable in the Terahertz Range," Proceedings of the 27th International Free Electron Laser Conference 2005, pp.87 -90

[47] T.J. Bridges and A.R. Strand, "Submillimeter wave generation by difference frequency mixing in GaAs, "Appl. Phys. Lett. **20**, 382-384 (1973)

[48] N.Lee, B. Lax, and R.L. Aggarwal, "High power far infrared generation in GaAs," Opt. Commun. **18**, 50 (1976)

[49] C.J. Johnson, G.H. Sherman, and R. Weil, "Far infrared measurement of the dielectric properties of GaAs and CdTe at 300K and 8K,"Appl. Opt. **8**, 1667-1671 (1969)

[50] F. Pedrotti and L. Pedrotti, Introduction to optics (Prentice Hall, New Jersey, 1993)

[51] A.G. Maki, C.C. Chou, K.M. Evenson, L.R. Zink, and J.T. Shy, "Improved molecular constants and frequencies for the CO_2 laser from new high-J and hot band frequency measurements, " J. Mol. Spectrosc. **167**, 211-224, (1994)

[52] V.G Dmitriev, G.G. Gurzadyan, and D.N. Nikogosyan, *Handbook of Nonlinear crystals* (Springer, 1997)

[53] S.Ya. Tochitsky, V.O. Petukhov, V.A. Gorobets, V.V. Churakov, and V.N. Jakimovich, "Efficient continuous-wave frequency doubling of a tunable CO_2 laser in $AgGaSe_2$," Appl. Optics **36**, 1882-1888 (1997)

[54] D. E. Evans, L.E. Sharp, B. W. James, and W. A. Peebles, "Far-infrared superradiant laser action in methyl fluoride," Appl. Phys. Lett., Vol. **26**, No. 11, pp. 630 (1975)

[55] L.Gordon, G.L. Woods, R.C. Eckardt, R.R. Route, R.S. Feigelson, M.M. Fejer and R.L. Byer, Electron. Lett. **29**, 1942 (1993)

[56] S. Ya. Tochitsky, S.E Trubnick, and C. Joshi, " Generation of THz pulses in Teflon bonded periodically inverted GaAs structures," Conference on Lasers and

Electro-Optics 2008 Technical Digest (Optical society of America, San Jose, 2008) CTuHH4

[57] E. A. J. Marcatili and R. A. Schmeltzer, "Hollow metallic and dielectric waveguides for long distance optical transmission and lasers," Bell Syst. Tech. J., vol. **43**, pp. 1783-1809 (1964)

[58] J.A. Stratton, "Electromagnetic Theory," McGraw-Hill Book Co., New York and London, 1941, p524

[59] M. Borghesi et al., "Guiding of a 10-TW picosecond laser pulse through hollow cappillary tubes," Phys. Rev. E. vol. 57, pp. 4899-4902 (1998)

[60] C. Sung, "Guiding of a High-Power CO_2 laser beam in a hollow waveguide," Master Thesis, UCLA (2004)

[61] B. Bowden, J. A. Harrington, O. Mitrofanov, "Silver/polystyrene-coated hollow glass waveguides for the transmission of terahertz radiation," Optics Letters, Vol. **32**, pp. 2945 (2007)

[62] G.W. Chantry, "The use of Fabry-Perot interferometers, etalons and resonators at infrared and longer wavelengths-an overview," *J. Phys. E: Sci. Instrum.* **15**, pp. 3-8 (1982)

[63] R. Ulrich, K. F. Renk, and L. Genzel, "Tunable sub-mm interferometers of the Fabry-Perot type," IEEE Trans. Microwave Theory Tech. **11**, pp. 363-371 (1963)

[64] J. R. Greig and J. Cooper, "Rapid scanning with the Fabry-Perot etalon," Appl. Opt. 7, pp. 2166- (1968)

[65] D. W. Porterfield, J. L. Hesler, R. Densing, E. R. Mueller, T. W. Crowe, and R. M. Weikle II, "Resonant metal-mesh bandpass filters for the far infrared," Appl. Opt. **33**, pp. 6046- (1994)

[66] R. Ulrich, "Far-infrared properties of metallic mesh and its complementary structure," Infrared Phys. 7, 37-55 (1967)

[67] Microtech Instruments, Inc. Website: http://www.mtinstruments.com/thzpolarizers

[68] W. C. Meecham, J. Appl. Phys. **27**, pp. 361 (1956)

[69] J. Pavageau and J. Bousquet, Opt. Acta **17**, 469 (1970)

[70] E. G. Loewen, M. Neviere, and D. Maystre, "Grating efficiency theory as it applies to blazed and holographic gratings," Appl. Opt. **16**, pp. 2711- (1977)

[71] H. Delsim-Hashemi, O. Grimm, J. Rossbach, H. et al., "Broadband single shot spectrometer," *Proceedings of the 27th International Free Electron Laser Conference,* Stanford, USA 2005, p. 514. (2005)

[72] B.E. Cole, J.B. Williams, B.T. King, M.S. Sherwin, and C.R. Stanley, "Coherent manipulation of semiconductor bits with terahertz radiation," Nature **410**, 60-63 (2001)

[73] S. Ya. Tochitsky, S. Reiche, C. Sung, J. B. Rosenzweig, C. Pellegrini, and C. Joshi, " Laser Beat-Wave microbunching of relativistic electron beam in the THz range," Proceedings of LINAC 2006, MOP029 (2006)

[74] D. Gordon, C.E. Clayton, T. Katsouleas et al, Phys. Rev. E, vol. **57**, pp.1035-1041 (1998)

[75] P. Sprangle *et al.*, Opt. Commun. **124**, pp.69 (1996)

[76] E. Esaray *et al.*, Phys. Rev. E **52**, pp.5443 (1995)

[77] S. Ya. Tochitsky, C.E. Clayton, K.A. Marsh, et al, AAC Proceeding 2004, pp. 663-669.

[78] S. Ya. Tochitsky, R. Narang, C. V. Filip, et al, " Experiments on laser driven beatwave acceleration in a ponderomotively formed plasma channel," Physics of Plasma, Vol. 11, pp. 2875 (2004)

[79] P. B. Corkum, A. J. Alcock, and Leopold K. E., "Electron-beam-controlled transmission of 10-m radiation in semiconductors," *Journal of Applied Physics*, 50:3079, (1979)

[80] P. Musumeci, S. Ya. Tochitsky, S. Boucher, C. E. Clayton, A. Doyuran, R. J. England, C. Joshi, C. Pellegrini, J. Ralph, J. B. Rosenzweig, C. Sung, S. Tolmachev, G. Travish, A. A. Varfolomeev, A. A. Varfolomeev Jr., T. Yarovoi, and R. B. Yoder, "High energy gain of trapped electrons in a tapered, diffraction-dominated inverse-free-electron-laser," Phys. Rev. Lett., 94, 154801 (2005)

[81] C. Sung, S. Ya. Tochitsky, S. Reiche, et al, " Seeded free-electron and inverse free-electron laser techniques for radiation amplification and electron microbunching in the terahertz range," Phys. Rev. ST Accel. Beams 9, 120703 (2006)